



# *In situ* characterisation of the strain fields of intragranular slip bands in ferrite by high-resolution electron backscatter diffraction

Abdalrhman Koko<sup>a,\*</sup>, Elsiddig Elmukashfi<sup>b</sup>, Thorsten H. Becker<sup>c</sup>, Phani S. Karamched<sup>a</sup>, Angus J. Wilkinson<sup>a</sup>, T. James Marrow<sup>a</sup>

<sup>a</sup> Department of Materials, University of Oxford, Oxford OX1 3PH, United Kingdom

<sup>b</sup> Department of Engineering Science, University of Oxford, Oxford OX1 3PJ, United Kingdom

<sup>c</sup> Centre for Materials Engineering, Department of Mechanical Engineering, University of Cape Town, Cape Town, South Africa

## ARTICLE INFO

### Article history:

Received 28 April 2022

Revised 14 August 2022

Accepted 17 August 2022

Available online 23 August 2022

### Keywords:

High angular resolution electron backscatter diffraction

Slip band

J-integral

Finite element analysis

Ferrite

Stress intensity factor

## ABSTRACT

High angular resolution electron backscatter diffraction has been used to quantify the local elastic field at the tip of mechanically loaded intragranular slip bands observed *in situ* in the ferrite grains of an age-hardened duplex stainless steel (Zeron 100). The surface elastic strain field was integrated to calculate in-plane and out-of-plane surface displacements. This allowed the elastic fields to be parameterised in a finite element analysis, which used the displacement field as the boundary conditions, to obtain the potential strain energy release rate (*J*-integral) and three-dimensional stress intensity factors ( $K_{I,II,III}$ ).

This new analysis method is demonstrated by examining the elastic fields around the tip of an incipient slip band, an array of slip bands and the loading of a slip band. Direct measurement of the stress tensor in the grain identified the active slip systems with the highest Schmid factor. The stress intensity factors ahead of the slip band, measured under load, were directly affected by the magnitude of loading and the inclination angle of the slip band to the observed surface.

© 2022 The Author(s). Published by Elsevier Ltd on behalf of Acta Materialia Inc.

This is an open access article under the CC BY license (<http://creativecommons.org/licenses/by/4.0/>)

## 1. Introduction

Deformation twins, slip bands and micro-cracks are deformation-induced features (DIFs) that can locally concentrate stress and strain in the microstructure of crystalline materials, particularly metals. Understanding their interactions, distribution, and accumulation is critical for the microstructural engineering of materials [1]. Few experimental studies have quantified the localised stress fields of DIFs, despite their importance to crystal plasticity finite element (CPFE) microstructure-sensitive models for mechanisms such as fatigue crack propagation [2–4] and deformation twin propagation [5]. CPFE can, to some extent [6], predict the local stress and strain distributions but currently omits finer details at the micro-scale [7–9]. The emerging phase-field approach is a promising way to simulate localised fields [10,11], and improved experimental methods to quantify the fields of DIFs, principally *in situ* studies, are needed to inform, validate, and calibrate such models.

The deformation field at the slip-band is due to three-dimensional elastic and plastic strains where the concentrated

shear of the slip band tip deforms the grain in its vicinity. The elastic strains describe the stress concentration ahead of the slip band, which is important as it can affect the transfer of plastic deformation across grain boundaries [12–14]. An understanding of this is needed to support the study of yield and inter/intra-granular fracture [15–17]. The concentrated shear of slip bands can also nucleate cracks in the plane of the slip band [18,19], and persistent slip bands that lead to intragranular fatigue crack initiation and growth may also form under cyclic loading conditions [20,21]. To properly characterise slip bands and validate mechanistic models for their interactions with microstructure, it is crucial to quantify the local deformation fields associated with their propagation. However, little attention has been given to slip bands within grains (i.e., in the absence of grain boundary interaction).

The long-range stress field (i.e., the elastic strain field) around the tip of a stress concentrator, such as a slip band, can be considered a singularity equivalent to that of a crack [22,23]. This singularity can be quantified using a path independent integral since it satisfies the conservation laws of elasticity. The conservation laws of elasticity related to translational, rotational, and scaling symmetries were derived initially by Knowles and Sternberg [24] from the Noether theorem [25]. Budiansky and Rice [26] introduced the *J*-, *M*-, and *L*-integrals and were the first to give them a physical

\* Corresponding author.

E-mail address: [abdo.koko@materials.ox.ac.uk](mailto:abdo.koko@materials.ox.ac.uk) (A. Koko).

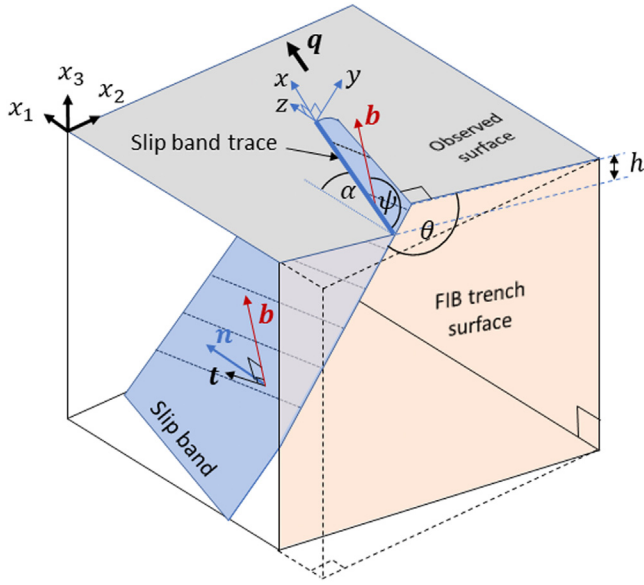


**Fig. 1.** Schematic of a slip band, relative to the measurement axes ( $x_1$ ,  $x_2$ , and  $x_3$ ), and axes related to the slip-band ( $x$ ,  $y$ , and  $z$ ), showing the angles that describe the relationship between these axes and the traces of the slip band ( $\alpha$ ,  $\theta$ ), and the inclination angle ( $\psi$ ) of the slip trace ( $x$ ) and Burgers vector ( $b$ ) relative to the surface.  $h$  is the slip band height, and  $q$  is the slip band propagation direction assumed for  $J$ -integral calculation when using the virtual extension method [60].  $t$  describes the line vector drawn here as for an edge dislocation, i.e.,  $b \perp t$ , and  $n$  is the slip band plane normal.

interpretation as the strain energy-release rates for mechanisms such as cavity propagation, simultaneous uniform expansion, and defect rotation, respectively. When evaluated over a surface that encloses a defect, these conservation integrals represent a configurational force on the defect [27]. That work paved the way for the field of configurational mechanics of materials [28,29], with the path-independent  $J$ -integral now widely used to analyse the configurational forces in problems as diverse as dislocation dynamics [30,31], misfitting inclusions [32], propagation of cracks [33], shear deformation of clays [34], and co-planar dislocation nucleation from shear loaded cracks [35]. The integrals have been applied to linear elastic and elastic-plastic materials and have been coupled with processes such as thermal [36] and electrochemical [37] loading, and internal tractions [38]. Experimental fracture mechanics studies have recently full-field *in situ* measurements of displacements [39,40] and elastic strains [41–43] to evaluate the local deformation field surrounding the crack tip as a  $J$ -integral.

Slip bands form due to plastic deformation, and the analysis of the force on a dislocation considers the two-dimensional nature of the dislocation line defect. General definitions of the Peach–Koehler configurational force ( $P_{kj}$ ) (or the elastic energy-momentum tensor [44]) on a dislocation in the arbitrary  $x_1$ ,  $x_2$ ,  $x_3$  coordinate system (Fig. 1), decompose the Burgers vector ( $b$ ) to orthogonal components [45]. This leads to the generalised definition of the  $J$ -integral in Eqs. (1) and (2). For a dislocation pile-up, the  $J$ -integral is the summation of the Peach–Koehler configurational force of the dislocations in the pile-up [45–47] (including out-of-plane,  $\vec{b}_3$  [48]).

$$J_k = \int_S P_{kj} n_j dS = \int_S (W_s n_k - T_i u_{i,k}) dS \quad (1)$$

$$J_k^x = R_{kj} J_j, \quad i, j, k = 1, 2, 3 \quad (2)$$

where  $S$  is an arbitrary contour around the dislocation pile-up with unit outward normal  $n_i$ ,  $W_s$  is the strain energy density,  $T_i = \sigma_{ij} n_j$  is the traction on  $dS$ ,  $u_i$  are the displacement vector components,  $J_k^x$

is  $J$ -integral evaluated along the  $x_k$  direction, and  $R_{kj}$  is a second-order mapping tensor that maps  $J_k$  into  $x_k$  direction. This vectorial  $J_k$ -integral leads to numerical difficulties in the analysis since  $J_2$  and, for a three-dimensional slip band or inclined crack, the  $J_3$  terms cannot be neglected.

This is also of practical importance in the direct asymptotic analysis of the geometrically induced singular stress concentrations at cracks and notches in elastic and inelastic materials [49]. Budiansky and Rice [26] and Hussain et al. [50] argued that for two-dimensional defects (i.e.,  $J_3$  neglected), the two components of the  $J_k$  vector represent specific energy release rates related to the movements of the crack surfaces along the  $x_1$ -axis and the  $x_2$ -axis, respectively. However, if we consider a contour enclosing a single crack tip, the calculated energy release includes the contribution to  $J_2$  arising from the traction-free surface. This will make  $J_2$  path dependent [51], although it can still be related to the stress intensity factors as shown in Eqs. (3) to (5) by treating  $J_k$  as vectors. With vectorial  $J_k$ , the values of  $K_{I,II,III}$  can be calculated using the Young's ( $E'$ ) and shear ( $\mu$ ) moduli but this method does not capture compressive fields; this is critical to the description of mode I loading. Thus, to simplify the  $J$ -integral analysis in a way that makes  $J_1$  precisely the energy release rate, whilst avoiding the difficulty of the physical interpretations of  $J_2$  and  $J_3$  [26],[49–54], the field can be resolved to a coordinate system consistent with the crack or slip band geometry and its direction of propagation. Note that typically, a 'three-dimensional'  $J$ -integral analysis in the finite element method is achieved as a series of two-dimensional approximations at nodes along the (curved or straight) crack front, dealing with the 3D field in layers of  $x_1$  and  $x_2$  that are one element thick [55–57]; thus,  $J_3$  is typically disregarded.

$$K_I = \frac{\sqrt{E'}}{2} \left[ \sqrt{J_1 - J_2 - J_3} + \sqrt{J_1 + J_2 - J_3} \right] \quad (3)$$

$$K_{II} = \frac{\sqrt{E'}}{2} \left[ \sqrt{J_1 - J_2 - J_3} - \sqrt{J_1 + J_2 - J_3} \right] \quad (4)$$

$$K_{III} = \sqrt{2\mu J_3} \quad (5)$$

The analysis of energy release rates cannot distinguish between the portions contributed by opening and shearing modes, which would be a disadvantage when studying mixed-mode crack propagation, for example. However, this singular  $J$ -integral can be related to the three-dimensional elastic stress intensity factors using a mode-decomposition technique such as the interaction integral method [58]. The elastic strain field may then be described in terms of mixed-modes of mode I (tensile/compression), mode II (in-plane shear) and mode III (out-of-plane shear). In fracture mechanics, their interactions can affect the direction of crack propagation [59]. In plasticity, quantifying the fields of slip bands to extract the magnitudes of the shear modes II and III may aid the interpretation of criteria for slip band propagation and interactions with microstructure features such as precipitates, inclusions, and grain boundaries.

This work aims to quantify the full elastic strain field around mechanically loaded slip bands, observed *in situ*, using high-resolution (HR) electron-backscatter diffraction (EBSD), which has the necessary spatial resolution and sensitivity to measure the field close to the surface. We have previously shown that the  $J$ -integral and decomposed stress intensity factors can be used to analyse the *in-plane* elastic strain field [61] of a surface observed by (HR)-EBSD. Here, the full elastic strain field is quantified using the  $J$ -integral (implemented in the finite element method) as a descriptor for the modes of deformation that contribute to the stress field. This paper describes the experimental methodology, the (HR)-EBSD analysis, and the finite element integration of the strain field to the

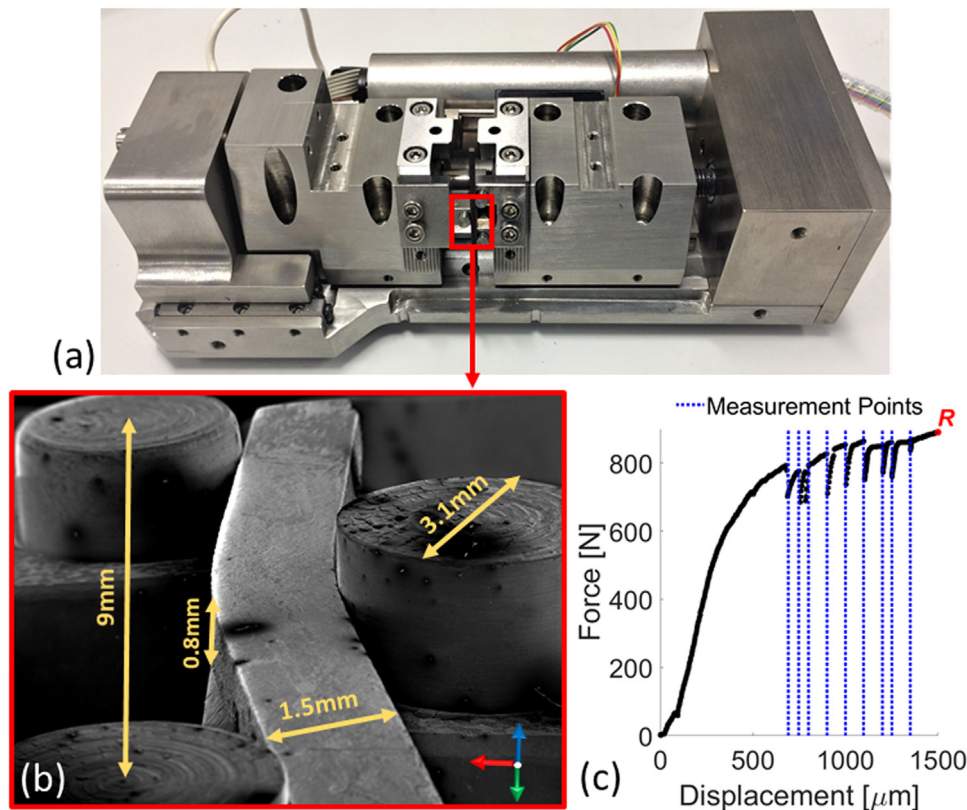


**Fig. 2.** (a) 2 kN Deben® 70° pre-tilted mechanical loading stage for *in situ* EBSD with (b) secondary electron image of the age-hardened duplex stainless-steel sample deformed in 3-point bending. (c) Applied force and measured displacement, with blue-dotted lines marking the *in situ* collections of electron backscatter diffraction maps. The sample was unloaded at point R for ex situ observation.

equivalent three-dimensional displacement field, from which the  $J$ -integral analysis is performed. With the assumption of small-scale plasticity, the  $J$ -integral is decomposed into the linear elastic stress intensity factors to express deformation modes. The analysis has been applied in a series of *in situ* studies in age-hardened ferrite (body-centred cubic) grains containing an incipient slip band, an array of slip bands, and the loading of a slip band.

## 2. Experimental method

### 2.1. Material and *in situ* mechanical deformation

The sample from a large ( $\sim 200$  mm thickness) forging of Zeron 100 duplex stainless steel (25% Cr, 7% Ni, 3.6% Mo, 0.7% Cu, 0.7% W, 0.22% N, wt.% nominal composition), measuring  $1.5 \times 12 \times 0.8$  mm<sup>3</sup>, was aged in the air at 475 °C for 100 h to induce hardening of the ferrite grains without change of the austenite structure (see supplementary information A). This encourages planar slip and twin formation in ferrite at room temperature [62–65]. This material was also chosen for its large ferrite grain size, around 0.25 mm<sup>2</sup>, with a volume fraction of 58%; (see supplementary information A). The surface for observation ( $1.5 \times 12$  mm<sup>2</sup>) was ground using silicon carbide papers (100 to 4000 grit), polished on medium (PSU-M) pads with Kemet diamond compounds (9 to 0.25  $\mu\text{m}$ ), then a Nap-type cloth with colloidal silica suspension for 1 h to mirror-finish, before ultrasonic cleaning for 20 minutes each in acetone, ethanol, and deionised water with final drying by hot air.

Mechanical deformation was done in 3-point bending (9 mm span) using a 2 kN Deben® 70° pre-tilted loading stage within a Carl Zeiss Merlin FEG-SEM. The chamber and stage were plasma

cleaned and purged for 15 h before testing the specimen at a displacement rate of 1 mm min<sup>−1</sup> (Fig. 2a and b). The test was paused (positions marked by dotted red lines in Fig. 2c) at fixed displacement to acquire electron backscatter patterns (EBSPs). The examined locations were selected by secondary electron (SE) and back-and-for-scatter electron (VFSD, Virtual Forward-scattered Electron Detector [66]) imaging. Given the sample dimensions and ferrite grain sizes, the selection of the slip bands to analyse was not influenced by the nominal distribution of strain and stress across the sample. Instead, the focus was on finding intragranular slip bands with a localised field that did not interact with other stress raisers, such as other slip bands, grain boundaries or phase boundaries.

*In situ* mapping was done by collecting an array ( $800 \times 600$ ) of EBSPs in a conventional EBSD setup employing a Bruker eFlash CCD camera with 10 nA/20 kV beam conditions, 100 millisecond exposure time per pattern,  $4 \times 4$  hardware pattern binning, and 75 nm step size. These conditions were selected as being practical with little drift [67,68], which give Kikuchi bands with sharp contrast [69], and adequate step size [70] and pattern binning [68] for dislocation type convolution. Some load relaxation (<13%) occurred during the pattern acquisition.

After a total applied monotonic displacement of 1.5 mm (red R in Fig. 2), selected slip bands were then sectioned by cutting trenches, orthogonally to their trace and the surface, using a Zeiss Auriga dual-beam SEM-FIB system that has a Schottky field emission Gemini electron column coupled with an Orsay Physics “Cobra” Ga<sup>+</sup> ion FIB with 1 nA/30 kV, after depositing a protective Pt layer on the surface at 240 pA/30 kV. The milled surface of the FIB trench wall (Fig. 1) was observed using in-lens secondary electron (SE) imaging.



## 2.2. High resolution (HR)-EBSD analysis

The diffraction of the backscattered electrons by the crystal's periodic lattice is observed as the Kikuchi bands of the electron backscatter pattern (EBSP) [71,72]. Deformation within the probed volume causes pattern degradation, pattern shift, and changes in the band widths [73]. In (HR)-EBSD, the EBSPs within each grain are cross-correlated with a reference EBSP (EBSP<sub>0</sub>) to measure the shifts and infer the elastic deformation gradient tensor [74,75]. Each EBSP was segmented into 30 regions of interest, normalised, and weighted to remove the background intensity gradients for cross-correlation. These were then fast Fourier transformed, filtered to remove low and high-frequency fluctuations (i.e., noise and background intensity gradients), and transformed back to the real domain before correlated with the reference pattern. To reduce the mean angular error (MAE) and increase the correlation peak height (PH), two iterations of the analysis were done, with the EBSPs remapped for the second iteration to the EBSP<sub>0</sub> orientation that was estimated from the first iteration [76]. An objective process selected the least strained reference pattern (i.e., the chosen EBSP<sub>0</sub>), using the empirical relation between MAE and PH to identify the reference pattern with the highest PH and lowest MAE [77].

The spatial maps were segmented into grains, using a 5° misorientation criteria, via MTEX [78]; this shows the ferrite grains are massive compared to the austenite and contain subgrains with low angle grain boundaries (>2°). These low-angle grain boundaries have a high geometrically necessary dislocation (GND) density due to low indexing from diffraction pattern overlaps as the probed volume extends across the boundary [79]. Choosing a reference pattern within these subgrains to perform (HR)-EBSD on the parent grain prominently affects the rotation components but does not influence the strain components due to the remapping on the 2nd iteration [76]. Pattern centre shifts due to beam movement during EBSP acquisition were minimised using AstroEBSD [80]. Changes in the sample topography do not affect the strain due to the remapping in the 2nd cross-correlation iteration [81] but may reduce the signal by shadowing in extreme cases [82].

The 3D elastic deformation tensor was inferred from the measured pattern shifts, with the assumption of zero stress normal to the surface [83] and was decomposed to the lattice rotation and elastic deviatoric strain at an estimated strain sensitivity of  $\pm 10^{-4}$  [84,85]. Deformation can affect the correlation quality and consequently the MAE by blurring the EBSP, so inadequate quality points (PH < 0.3 and MAE >  $10^{-3}$  rad [82]) were removed from the map. These did not exceed 0.1% of the map area in all cases.

## 2.3. Local Schmid factor by (HR)-EBSD

For interpretation of the plastic deformation, it is helpful to determine the Schmid factor for each slip system in the grain. This requires knowledge of the stress acting within the grain. Uniaxial stress cannot be assumed due to the multiaxial deformation of the plastic bending of the beam, but knowledge of the full elastic stress field is obtained in the sample frame using (HR)-EBSD. The GND density may be used to identify strain concentrations, and such outliers, including the sub-grain boundary, were removed from the stress map. Using the remaining points (<40% of the total), the normalised mean values of the stress components remaining points (<40% of the total), the normalised mean values of the stress components (i.e.,  $\sum \|\sigma_{ij}\| = 1$ ) were used to determine the local stress state of the grain. The matrix of the normalised stress components was rotated to the crystal frame using a rotation matrix ( $R_{\varphi_1, \Phi, \varphi_2}$ ) constructed from the Euler angles ( $\varphi_1, \Phi, \varphi_2$ ) of the reference pattern (EBSP<sub>0</sub>), as in Eq. (6), to construct a loading direction matrix ( $r$ ), as in Eq. (7). From this, the (HR)-EBSD-

based Schmid factor (xSF) in the grain was calculated, using MTEX [86], for the  $i$ th slip system's plane normal ( $n^{(i)}$ ) and shear direction ( $d^{(i)}$ ), which is parallel to the Burgers vector ( $b$ ). These were ranked according to their probability of occurrence, which was determined by the magnitude of the Schmid factor. The supplementary information B provides an extended introduction to this analysis with other examples.

$$R_{\varphi_1, \Phi, \varphi_2} = \begin{bmatrix} \cos \varphi_2 & -\sin \varphi_2 & 0 \\ \sin \varphi_2 & \cos \varphi_2 & 0 \\ 0 & 0 & 1 \end{bmatrix} \begin{bmatrix} 1 & 0 & 0 \\ 0 & \cos \Phi & -\sin \Phi \\ 0 & \sin \Phi & \cos \Phi \end{bmatrix} \times \begin{bmatrix} \cos \varphi_1 & -\sin \varphi_1 & 0 \\ \sin \varphi_1 & \cos \varphi_1 & 0 \\ 0 & 0 & 1 \end{bmatrix} \quad (6)$$

$$r = \|R_{\varphi_1, \Phi, \varphi_2} \sigma_{ij} R_{\varphi_1, \Phi, \varphi_2}^T\| \quad (7)$$

$$xSF_i = \frac{r \cdot n^{(i)}}{|r| |n^{(i)}|} \cdot \frac{r \cdot d^{(i)}}{|r| |d^{(i)}|} \quad (8)$$

## 2.4. Resolving the strain field to the slip-band frame of reference

The elastic deviatoric strain field, obtained in (HR)-EBSD analysis using measured shifts and distortions between EBSPs and a reference EPSP, was integrated into its equivalent displacement field to enable  $J$ -integral analysis by the finite element method. The analysis was simplified by performing a rotational transformation of the elastic strain tensors obtained from (HR)-EBSD to resolve them to the slip band geometry using a  $Q_z(\alpha)$  and  $Q_x(\theta)$ ; thus, making  $x$  and  $y$  the horizontal and vertical axes of the image frame, respectively. The necessary angles (Fig. 1) were obtained by EBSD-based trace analysis [87] of the slip band at the specimen surface and on the orthogonal wall of a focused ion beam (FIB)-milled trench on which the sub-surface slip trace was observed by secondary electron microscopy. These transformations resolve the strain field to the slip band, thus  $J_3$  is directly equivalent to the out-of-surface energy release rate ( $G^{III}$ ) since the slip band normal is perpendicular to the slip trace on the surface ( $x_3 \perp q$ ).

$$Q_z(\alpha) = \begin{bmatrix} \cos \alpha & \sin \alpha & 0 \\ -\sin \alpha & \alpha & 0 \\ 0 & 0 & 1 \end{bmatrix} \quad (9)$$

$$Q_x(\theta) = \begin{bmatrix} 1 & 0 & 0 \\ 0 & \cos \theta & \sin \theta \\ 0 & -\sin \theta & \cos \theta \end{bmatrix} \quad (10)$$

$$\varepsilon' = Q_\varepsilon Q^T \quad (11)$$

The slip band resolved axes,  $x$ ,  $y$ , and  $z$ , are shown in comparison with the sample observation axes,  $x_1$ ,  $x_2$ , and  $x_3$  in Fig. 1. The sample axes,  $x_1$ ,  $x_2$ , and  $x_3$ , are shown in all figures in this chapter using blue, red, and green arrows, whereas  $x$  and  $y$  refer the image/frame axes (horizontal and vertical, respectively) that are resolved to the slip band.

## 2.5. (HR)-EBSD depth of information

The electron beam of the Merlin FEG-SEM has an averaged mean-radius at the specimen surface of about  $\sim 25$  nm at the 20 kV/10 nm beam condition [88]. The elliptical intersection of the beam on the 70° tilted surface means that the longitudinal resolution is 3 times higher than the lateral [89]. This geometry was used in a Monte Carlo (MC) simulation (Casino v2.48 [90]) of the trajectories of  $5 \times 10^6$  electrons into a bulk ferrite phase of 25% Cr, 5.4% Ni, 3.9% Mo, 0.6% Mn, 0.6% Cu, wt.% nominal composition [91]. The simulation was used to determine the probability

for electrons to backscatter to the surface from a certain depth. The effective (mean) depth of information (50% probability) was thus estimated to be approximately 46 nm (See supplementary information A), which defined the membrane finite element model used to analyse the  $J$ -integral from the deformation field.

## 2.6. $J$ -integral and three-dimensional stress intensity factors

The finite element method was used to obtain the displacement field from the measured elastic strains and extract the  $J$ -integral and three-dimensional stress intensity factors. To obtain the displacement field, a finite element model was defined in MATLAB® using hexahedron (brick) elements with 8 nodes to structurally mesh a 3D volume of 46 nm thickness (i.e., the (HR)-EBSD probed membrane layer). As an approximation, it was assumed that the plane of the slip band was perpendicular to the thin membrane by considering the rotational transformations of the stress field executed earlier. The coordinates of the nodes and element connectivity matrix were used to calculate the shape function and Jacobian for isoparametric linear brick elements with 8 Gauss points (full integration). The concept of the analysis is to use the shape/interpolation function to relate the strain at the measurement point (centric point) to the Gauss integration points and then to the (integrated) nodal displacement. The element stiffness and force matrix at the Gauss points were assembled in a sparse matrix for efficient memory use. The nodal displacements were solved via the MATLAB® *lsqminnorm* algorithm, suitable for sparse matrixes and computationally inexpensive [92]<sup>1</sup>. The resultant nodal displacements were corrected for rigid body movement (translations and rotation), and the point with absolute minimum displacement was defined as the origin [93]. These integrated displacement fields may be regarded as similar to those obtained by stereo digital image correlation (3D DIC) [94] since the analysis gives information of the in-plane and out-of-plane movements of the surface.

The elastic displacements ( $u$ ) at the nodes were then examined using a mode-decomposition technique [56],[95–99] that separates the field into components of symmetric ( $u^I$ ), in-plane anti-symmetric ( $u^{II}$ ) and out-of-plane anti-symmetric ( $u^{III}$ ) fields by superimposing an auxiliary field onto the actual field with mirroring along the  $x_1$ -axis (Eq. (12)). The auxiliary field was used to enlarge the actual field, forming a representation of symmetry while satisfying both the equilibrium equation and an assumed traction-free boundary condition on the slip plane surface (detailed in [100]).

$$u = u^I + u^{II} + u^{III} = \frac{1}{2} \begin{Bmatrix} u_x + \bar{u}_x \\ u_y - \bar{u}_y \\ u_z + \bar{u}_z \end{Bmatrix} + \frac{1}{2} \begin{Bmatrix} u_x - \bar{u}_x \\ u_y + \bar{u}_y \\ 0 \end{Bmatrix} + \frac{1}{2} \begin{Bmatrix} 0 \\ 0 \\ u_z - \bar{u}_z \end{Bmatrix} \quad (12)$$

$$u = u^I + u^{II} + u^{III} = \frac{1}{2} \begin{Bmatrix} u_x + \bar{u}_x \\ u_y - \bar{u}_y \\ u_z + \bar{u}_z \end{Bmatrix} + \frac{1}{2} \begin{Bmatrix} u_x - \bar{u}_x \\ u_y + \bar{u}_y \\ 0 \end{Bmatrix} + \frac{1}{2} \begin{Bmatrix} u_z + \bar{u}_z \\ 0 \\ u_z - \bar{u}_z \end{Bmatrix} \quad (13)$$

The potential strain energy release rate ( $J^{I,II,III}$ ) and corresponding stress intensity factors for each decomposed field were evaluated using the ABAQUS® finite element solver by applying the nodal displacements of each of the  $u^I$ ,  $u^{II}$  and  $u^{III}$  fields as boundary conditions for a two-dimensional geometry, as simplified in Eq. (13). The  $u^I$  and  $u^{II}$  fields provide  $K_I$  and  $K_{II}$ . By considering the fields in this way, there is no need to assume that  $u_z + \bar{u}_z = 0$ ; that assumption has been made previously where 3D stereo-DIC

surface measurements [101] (citing [102]) provided only the two-dimensional displacements. For  $u^{III}$ , by using the mode decomposition algorithm implemented in ABAQUS, we can calculate the anti-symmetric shear  $K_{III}$  and its associated symmetric out-of-plane mode I contribution (i.e.,  $K_I^r$ ).

The calculations were executed while maintaining the same rectangular grid spacing with 4 nodes for each plane stress element (ABAQUS® CPS4). The slip band was defined with its tip position located within the displacement field using the information from the maps of GND density and VFSD images, which had a precision of ~75 nm. The application of ABAQUS as the FE solver also allows the use of linear elastic, anisotropic elastic, and elastoplastic material properties and the implementation of equivalent domain integration (EDI) [55,57,60], rather than line integration, to calculate the magnitude and sign of the three-dimensional stress intensity factors [103]. The EDI starts at the slip band tip and propagates in the local direction of a virtual extension with the linear spatial variation across nodes calculated using a smoothing function ( $q$ ) that equals unity at the tip and zero outside the domain.

In the present elastic analysis, the anisotropic linear elastic properties of the ferrite crystal were used, and the slip band was defined as a traction-free surface (i.e., an equivalent crack) orthogonal to the membrane. The stiffness matrix was calculated by rotating the ferrite orthotropic stiffness tensor ( $C_{11} = 230$ ,  $C_{44} = 117$ ,  $C_{12} = 135$  in GPa [104]) to the crystal orientation of the EBSP<sub>0</sub> [105]. A rotation matrix ( $R_{\varphi_1, \Phi, \varphi_2}$ ) was constructed from the Euler angles ( $\varphi_1$ ,  $\Phi$ ,  $\varphi_2$ ) of the reference pattern (EBSP<sub>0</sub>) as below [106–109] following the conventional EBSD rotation  $Z' X' Z''$  scheme [110] that is summarised in Eq. (14). By using the rotation matrix, the anisotropic elastic stiffness matrix,  $C_{EBSP_0}$ , was mapped from the reference crystal coordinate system to the local coordinate system [111,112].

$$R_{\varphi_1, \Phi, \varphi_2} = R_z(\varphi_2)R_x(\Phi)R_z(\varphi_1) \quad (14)$$

As noted above, the resultant  $J$ -integral and stress intensity factor values obtained using the  $u^I$  displacement field gives  $J^I$  and  $K_I$ , whereas the  $u^{II}$  displacement field gives  $J^{II}$  and  $K_{II}$ . The  $u^{III}$  displacement field gives the anti-symmetric out-of-plane shear,  $K_{III}$ , and the symmetric out-of-plane,  $K_I^r$ , components (Eq. (15)). Moreover, Cottrell and Rice [113] showed that for mixed-mode crack loading, the total strain energy release rate,  $J$ , is the sum of the energy release rates for each mode, as in Eq. (16). The code for this analysis and benchmarking datasets are available at [10.5281/zenodo.6411569](https://doi.org/10.5281/zenodo.6411569). The supplementary information C provides an analysis of the errors for this method.

$$K_I^r = K_I + K_I^r \quad (15)$$

$$J = J^I + J^{II} + J^{III} \quad (16)$$

## 3. Results and discussion

The analyses were applied to a series of *in situ* observations, comprising an incipient slip band, an array of slip bands, and a slip band studied under an increasing load to investigate their stress fields. During deformation, the austenite phase first showed planar slip, with secondary slip developing as the applied displacement was increased. In ferrite, wavy slip was observed, accompanied by linear deformation bands that mostly terminated at grain or phase boundaries (Fig. 3). These could be readily distinguished as deformation twins and slip bands using VFSD imaging, as in the far-field condition (38 mm working distance) the CCD camera diodes have high sensitivity to changes in diffraction angle [66,114]; the change in orientation of twins gives colour contrast, whereas the local plastic deformation of slip bands gives higher intensity contrast (i.e., highly-saturated, or low-intensity pixels). As

<sup>1</sup> Code with example is available at <https://doi.org/10.5281/zenodo.6411573>.

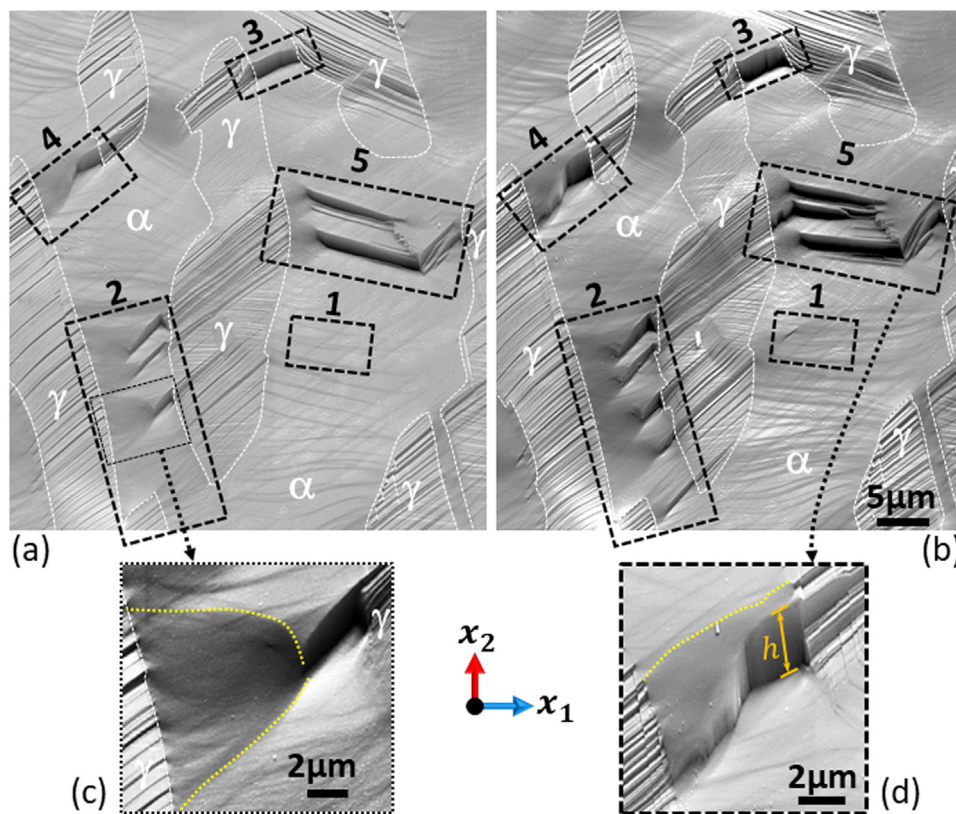


**Fig. 3.** Secondary electron images of age-hardened duplex stainless-steel observed *in situ* in three-point bending at applied crosshead displacements of (a) 1.2 mm and (b) 1.5 mm. Selected regions (2 and 4) are shown with higher magnification in (c) and (d). The apparent slip band height is marked as 'h'. Ferrite ( $\alpha$ ) and austenite ( $\gamma$ ) phases are labelled.

loading progressed, there was an increase in the amount of wavy slip (Fig. 3, box 1), an increase in the number of slip bands in ferrite (Fig. 3, box 2), and an increase in the width (i.e., height) 'h' of slip steps (Fig. 3, box 3). The slip band propagation was accompanied by increased step height (Fig. 3, box 4) with a smooth or sharply kinked transition to slip systems of different orientations in an adjacent grain (Fig. 3, box 5). Some slip bands terminated at sub-grain boundaries (misorientation  $< 1^\circ$ ), and others terminated mid-grain with no apparent obstacle.

### 3.1. Incipient slip band

An array of parallel slip bands in a ferrite subgrain,  $\alpha_1$ , is shown in Fig. 4a. The slip bands are blocked by a low-angle grain boundary (misorientation  $< 1^\circ$ ). The secondary electron image shows a 'bloom-like' contrast variation at each of the blocked slip band tips, indicating a gradual change in height that accommodates the out-of-plane shear displacement of the slip band; the latter is apparent from the sharp height change within the subgrain  $\alpha_1$ . A small step-like feature has also developed parallel to the slip traces within the adjacent subgrain  $\alpha_2$ . Analysis of the grain orientation by EBSD [115] shows its trace is consistent with the (112) slip plane that is inclined at  $\sim 90^\circ$  to the surface (Fig. 5a). This was confirmed via sectioning by focused ion beam (FIB) milling and secondary electron (SE) imaging observation. The step is, thus, on a slip band that is nearly normal ( $89 \pm 1^\circ$ ) to the specimen surface (Fig. 4c).

If the simple normal stress in the direction of maximum bending moment ( $x_1$ -axis direction) were assumed to act within the subgrain, the expected slip system with maximum shear stress would be  $[1\bar{1}1](110)$  (Table 1). However, this is not consistent with the observed plane. A loading direction matrix ( $L_c$ ) was constructed from the (HR)-EBSD stress field of subgrain  $\alpha_2$ , as described in

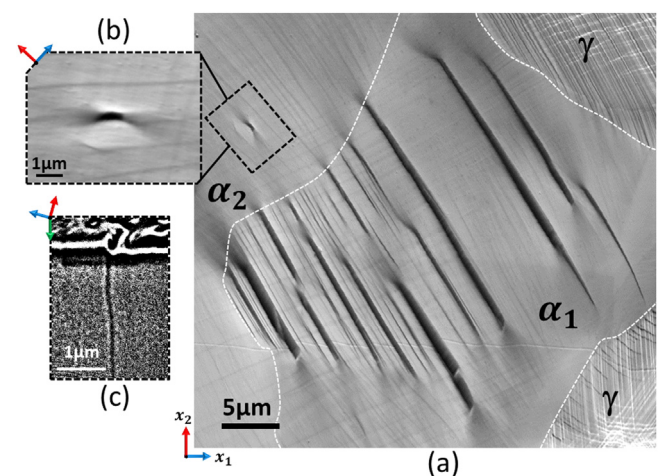


**Fig. 4.** (a) SEM image of an array of slip bands and (b) (112) trace and (c) focused ion beam trench wall in a ferrite grain of age-hardened duplex stainless steel.

Section 2.3, and it was found that the  $[11\bar{1}](112)$  slip system has the highest Schmid factor of the  $\{112\}$  planes (Table 1). Its trace is within  $2^\circ$  of the observed slip band and the other parallel slip traces in this grain. This analysis demonstrates the importance of knowledge of the stress state to define the local Schmid factor [116].

The EBSD analysis provides the crystallographic directions of the slip band trace (i.e.,  $x$ -axis in Fig. 1, which is perpendicular to both the slip band plane normal,  $n$ , and sample surface normal) and the local Schmid factor analysis also provides the expected shear direction of the Burgers vector ( $b$ ) of the most highly



**Table 1**

Slip variants (see Fig. 5b) with the relative Schmid factor (1 is highest), calculated with the assumption of (i) tensile loading ( $x_1$ ) and (ii) local stress state of the grain (xSF). Systems ('v' and 'w') with traces parallel to that of the observed slip band in the subgrain  $\alpha_2$  are bold. The system ('v') with the highest Schmid factors is highlighted with a double-lined square. EBSD maps are in the supplementary information A.

Label	Trace	$x_1$	xSF	Label	Trace	$x_1$	xSF	Label	Trace	$x_1$	xSF
a	$[\bar{1}\bar{1}\bar{1}](110)$	1	22	i	$[\bar{1}\bar{1}\bar{1}](2\bar{1}\bar{1})$	10	15	q	$[\bar{1}\bar{1}\bar{1}](\bar{1}\bar{1}\bar{2})$	14	10
b	$[\bar{1}\bar{1}\bar{1}](110)$	20	7	j	$[\bar{1}\bar{1}\bar{1}](21\bar{1})$	5	19	r	$[\bar{1}\bar{1}\bar{1}](\bar{1}\bar{1}\bar{2})$	21	14
c	$[\bar{1}\bar{1}\bar{1}](211)$	18	3	k	$[\bar{1}\bar{1}\bar{1}](\bar{1}\bar{2}\bar{1})$	4	21	s	$[\bar{1}\bar{1}\bar{1}](011)$	6	11
d	$[\bar{1}\bar{1}\bar{1}](101)$	9	5	l	$[\bar{1}\bar{1}\bar{1}](\bar{1}\bar{1}0)$	3	24	t	$[\bar{1}\bar{1}\bar{1}](011)$	16	1
e	$[\bar{1}\bar{1}\bar{1}](101)$	17	5	m	$[\bar{1}\bar{1}\bar{1}](\bar{1}\bar{1}0)$	15	12	u	$[\bar{1}\bar{1}\bar{1}](121)$	2	18
f	$[\bar{1}\bar{1}\bar{1}](1\bar{1}\bar{2})$	19	8	n	$[\bar{1}\bar{1}\bar{1}](2\bar{1}\bar{1})$	7	20	v	$[\bar{1}\bar{1}\bar{1}](112)$	11	2
g	$[\bar{1}\bar{1}\bar{1}](0\bar{1}\bar{1})$	8	17	o	$[\bar{1}\bar{1}\bar{1}](10\bar{1})$	12	16	w	$[\bar{1}\bar{1}\bar{1}](12\bar{1})$	23	9
h	$[\bar{1}\bar{1}\bar{1}](0\bar{1}\bar{1})$	22	23	p	$[\bar{1}\bar{1}\bar{1}](10\bar{1})$	13	13	x	$(\bar{1}\bar{2}1)[\bar{1}\bar{1}\bar{1}]$	24	4

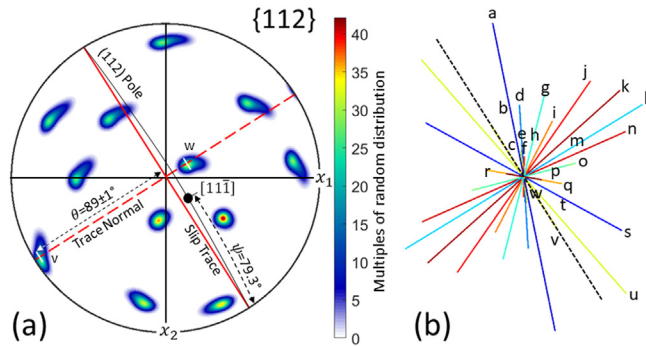


**Fig. 5.** (a)  $\{112\}$  pole figure obtained for the ferrite subgrain  $\alpha_2$ , generated using MTEX [117] as a stereographic projection. The slip band trace (solid red line) and the projection of the trace normal on the equatorial plane (dotted red line) are shown. The poles of the (112) and (121) planes are marked by 'v' ( $89 \pm 1^\circ$  from the surface normal) and 'w' ( $13 \pm 1^\circ$  from the surface normal), respectively (see Table 1), and the  $[\bar{1}\bar{1}\bar{1}]$  direction in (112) is also labelled. (b) Traces of the possible slip systems for this ferrite grain (see Table 1). The trace length is proportional to the Schmid factor, calculated from the local stress tensor. The surface trace of the observed slip band is shown as a dashed black line, which is parallel to the traces of (112) and (121).

stressed slip system of the slip band. Together, these provide the information required to calculate the slip inclination angle ( $\psi$ ) [118] (Fig. 1). For the  $[\bar{1}\bar{1}\bar{1}](112)$  slip band,  $\psi$  is  $79.3 \pm 1.4^\circ$ , which is consistent with the significant height of the slip band steps in the subgrain  $\alpha_1$  that has essentially the same crystal orientation as subgrain  $\alpha_2$ . The step-like feature in subgrain  $\alpha_2$  is therefore identified as an incipient slip band where the diffuse deformation (indicated by the multiple slip traces with low surface profile elsewhere in the subgrain) has become localised, with a significant out-of-plane shear due to the high slip inclination angle. With continued deformation, it would be expected to develop to a more extended slip band such as observed in subgrain  $\alpha_1$ .

The (HR)-EBSD data and the integrated in-plane elastic displacement field were resolved and rotated to align the incipient slip band with the horizontal  $x$ -axis of the (HR)-EBSD maps; these show the effect of the surface stretching accommodates the out-of-plane shear of the slip band (Fig. 6). The highest strains exist at the slip band tips. The integrated elastic displacements show opposing  $U_x$  displacements at each tip (i.e., shear) with a positive  $U_y$  gradient across the grain (i.e., tension). The out-of-plane  $U_z$  elastic displacement field also shows a step-change in height consistent with the topography, although the calculated elastic displacement is significantly smaller than the observed plastic displacement in Fig. 4c.

The strain energy field around the incipient slip band was then evaluated. The  $J$ -integral is only appropriate for strain energy release rate analysis of one singularity, so the  $J$ -integral was evaluated by independently considering the tips of the slip band.

This was done by splitting the measured field at its centre along the vertical axis. The  $q$  vectors (Fig. 7a) were chosen to parallel the slip band trace, and the integration domain was expanded in  $\sim 100$  nm intervals. Stable convergence of the  $J$ -integral was achieved for both ends of the slip band once the displacement singularity was engulfed by the integration domain (Fig. 7b). The initial non-convergence of the  $J$ -integral can be due to the breakdown of the elasticity assumption and close to the slip band tip, i.e., an elevated level of localised plasticity (Fig. 6) [27]. Convergence also began to fail when the domain expanded to interact with the peripheral fields of other stress raisers, such as the array of slip bands in the adjacent subgrain. Their contribution to the gradient field makes the vector field non-conservative (path independent) unless fully engulfed by the integration domain [48,119].

The characteristic  $J$ -integral values were taken as the average from the stable converged region (shaded area in Fig. 7I and II), with the variance indicating the convergence stability. The  $J$ -integrals at either end of the slip band are  $0.82 \pm 0.03 \text{ J m}^{-2}$  and  $0.51 \pm 0.00 \text{ J m}^{-2}$ . Decomposition to stress intensity factors show the stress field singularity is equally dominated by opening in-plane mode I ( $0.25 \pm 0.01 \text{ MPa m}^{0.5}$  and  $0.21 \pm 0.01 \text{ MPa m}^{0.5}$ ) and opposing mode III out-of-plane shears ( $0.21 \pm 0.01 \text{ MPa m}^{0.5}$  and  $-0.11 \pm 0.01 \text{ MPa m}^{0.5}$ ). The mode II in-plane shear is small ( $0.05 \pm 0.01 \text{ MPa m}^{0.5}$  and  $0.01 \pm 0.00 \text{ MPa m}^{0.5}$ ). The small symmetrical out-of-plane (compressive) contribution to mode I ( $K_I^r$  in Eq. (15)) is neglected ( $-0.01 \text{ MPa}$  and  $0.00 \text{ MPa m}^{0.5}$ ). The (negative) sign of the in-plane  $K_{II}$  and out-of-plane  $K_{III}$  shear depends on the chosen arrangement of the nodes at the tip and does not carry any physical meaning [120]. The incipient slip band formed an out-of-plane step with its shear direction ( $\psi$  at  $79.3^\circ$  to the surface trace) in a slip plane that is practically normal to the surface; this shear would be expected to lead to a high mode III stress intensity factor with negligible mode II. The mode I stress intensity factor is deduced to be due to the surface stretching necessary to accommodate the emergence of the step.

In summary, the analysed feature is an incipient slip band where plastic deformation has started to localise to cause a step-like feature with a shear displacement out of the surface. The dominant slip system is consistent with the (HR)-EBSD-based Schmid factor (xSF) in the grain, which was determined by local analysis of the stress tensor. The analysis to parameterise the elastic strain field has shown how the surface deforms to accommodate the shearing of this step, leading to the observed mode I and III stress intensity factors.

### 3.2. An array of slip bands

An array of slip bands within a ferrite grain is shown in Fig. 8. A 'blooming zone' of diffuse slip can be observed at the tip of each of these slip bands. The blooming zone increased in size as the load was increased and was also accompanied by a gradual increase in

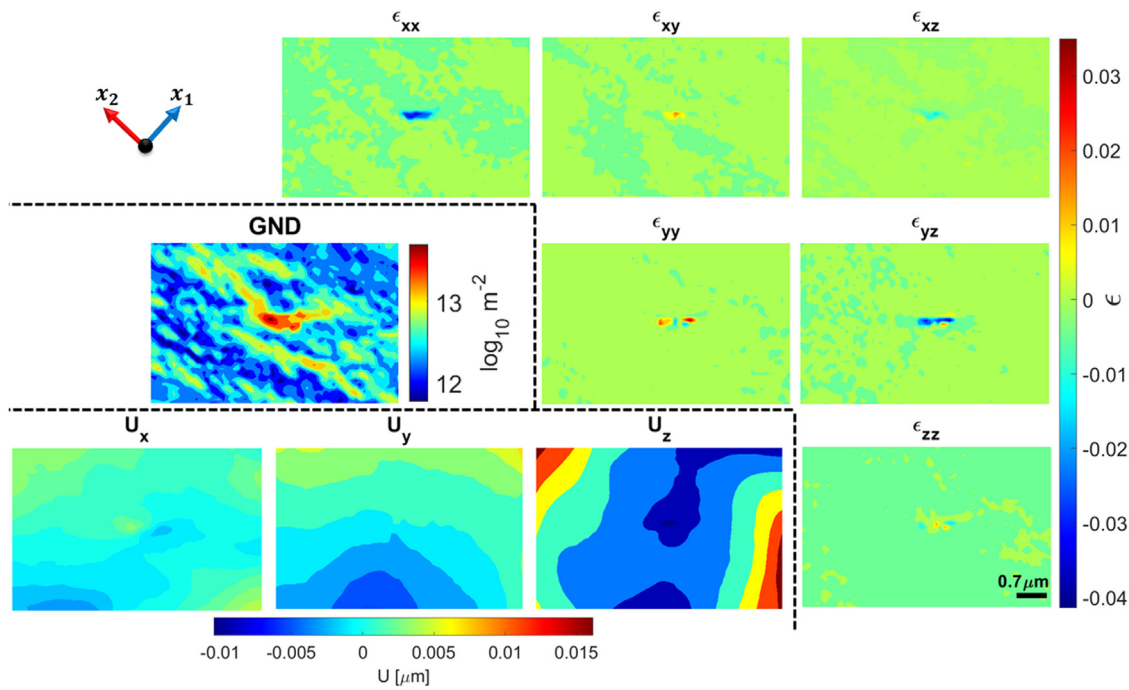


Fig. 6. Components of the elastic deformation field of  $[11\bar{1}](112)$  slip band, which is located at the figure centre.

Table 2

Field parameters calculated for the  $[11\bar{1}](\bar{1}12)$  slip band array. The symmetrical out-of-plane contribution to mode I is noted as  $K_I^r$ . The total mode I stress intensity factor ( $K_I^T$  in Eq. (15)) is the summation of the in-plane mode I ( $K_I$ ) and  $K_I^r$ . The negative sign of the in-plane  $K_{II}$  and out-of-plane  $K_{III}$  shear depends on the arrangement of the nodes at the tip and does not carry any physical meaning [120]. Accounting for the slip plane inclination,  $\theta$ , the slip step height is  $\sim 170\%$  of the measured thickness.

Label	Thickness ( $\mu\text{m}$ )	$J$ ( $\text{J m}^{-2}$ )	$K_I$ ( $\text{MPa m}^{0.5}$ )	$K_{II}$ ( $\text{MPa m}^{0.5}$ )	$K_{III}$ ( $\text{MPa m}^{0.5}$ )	$K_I^r$ ( $\text{MPa m}^{0.5}$ )	$K_I^T$ ( $\text{MPa m}^{0.5}$ )
2	$0.61 \pm 0.02$	$5.10 \pm 0.08$	$1.20 \pm 0.05$	$0.50 \pm 0.03$	$-0.69 \pm 0.03$	$-0.15 \pm 0.06$	$1.05 \pm 0.08$
1	$0.59 \pm 0.02$	$2.98 \pm 0.08$	$0.91 \pm 0.01$	$0.15 \pm 0.03$	$-0.29 \pm 0.07$	$-0.21 \pm 0.02$	$0.70 \pm 0.02$
3	$0.44 \pm 0.01$	$0.84 \pm 0.02$	$0.37 \pm 0.03$	$0.10 \pm 0.00$	$-0.15 \pm 0.02$	$-0.06 \pm 0.03$	$0.31 \pm 0.04$

the slip band length and its apparent width, i.e., height (Fig. 8d). The average slip band widths (Table 2) were measured on the surface SEM image and GND density map (Fig. 9b) at a 1.1 mm extension. FIB sectioning orthogonal to the trace of one of the slip bands found that the slip plane is inclined by  $60 \pm 1^\circ$  to the surface ( $\theta$  in Fig. 1). The surface trace analysis with the EBSD measurements of grain orientation, where the local Schmid factor ( $xSF$ ) was calculated via the stress field from (HR)-EBSD (see supplementary information B), identified the array as  $[11\bar{1}](\bar{1}12)$  slip bands with a slip inclination angle ( $\psi$ ) of the Burgers vector that was  $107.6 \pm 9.5^\circ$  from the surface trace (i.e., significant out of the surface shear).

The elastic strain field was resolved to the slip band plane and integrated for the equivalent displacements. These are presented in Fig. 9 and have the highest magnitude for the thickest slip band (Table 2), where thickness is a proxy for the step height of the inclined slip band. There is a clear step in the in-plane  $U_x$  and out-of-plane  $U_z$  elastic displacements across the slip band, which increases with the slip band height. The opening  $U_y$  displacement is more concentrated around the thinner slip band (i.e., smallest height step).

The  $J$ -integral analysis with mode decomposition to stress intensity factors was applied to the integrated elastic displacement fields, with a distance between consecutive contours of  $\sim 75$  nm (supplementary information A). The analysed region was chosen to exclude the deformation fields from neighbouring slip bands. The magnitude of all the strain field parameters is highest for the thicker slip bands (Table 2), and the mode II and III stress inten-

sity factors were similar. The existence of both shear modes is expected since the Burgers vector of the slip band describes shear in a direction at a high inclination angle ( $\psi$  at  $\sim 107^\circ$ , measured within the slip plane) from the surface trace, where the slip plane ( $\theta$ ) is at  $\sim 60^\circ$  to the surface. The mode I stress intensity factor, including the small contribution from out-of-plane deformation, has the highest magnitude. As with the incipient slip band, the tensile mode I stress intensity factor arises from stretching the surface membrane that accommodates the increase in slip step height. Note that the sign of in-plane and out-of-plane shear (mode II and III) is considered irrelevant as it depends on the arrangement of the nodes at the tip and does not carry any physical meaning [120]; however, the sign of mode I is critical as it describes the tensile or compressive conditions that exist at the slip band tip. The sign of the symmetrical out-of-plane contribution to mode I ( $K_I^r$ ) is not dependent on the sign of the mode III stress intensity factor.

In summary, the analysis in this section has shown there is an effect of slip band height on the stress field by examining an inclined array of parallel slip bands under the same state of loading that established the highest Schmid factor on the  $[11\bar{1}](\bar{1}12)$  slip system. The magnitudes of the elastic field and integrated displacements increase with the slip band height, showing how the surface membrane deforms to accommodate the localised shear of the slip band. The elastic fields at the slip band tips, parametrised using the  $J$ -integral and stress intensity factors, have significant components in modes II and III. This is consistent with the inclination angle of the shear direction in the slip bands.



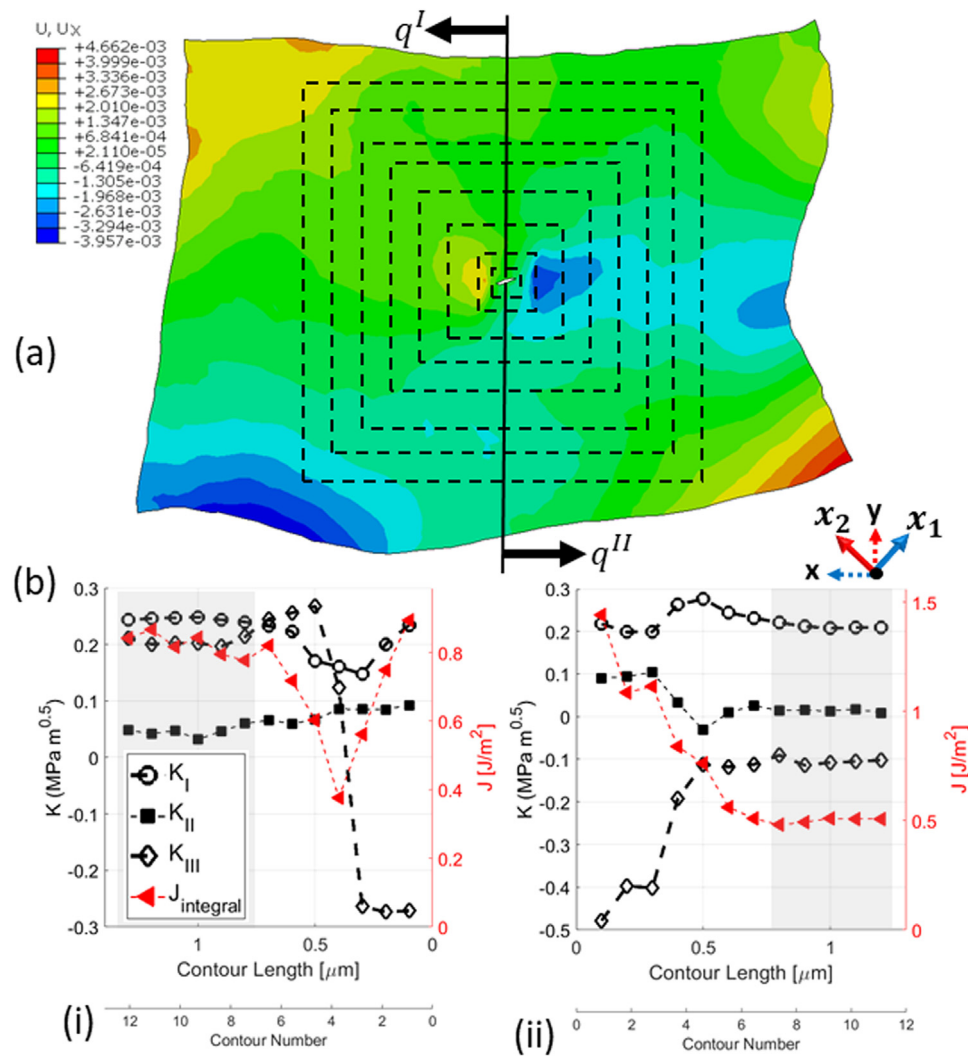


**Fig. 7.** (a) The deformed configuration (exaggerated, with colour contours showing only the  $U_x$  component of the displacement field) around the feature on the  $[11\bar{1}](112)$  slip band with expanding EDI (dashed squares). (b)  $J$ -integral analysis was conducted at both ends of the feature using opposing vectors,  $q^I$  and  $q^{II}$ .

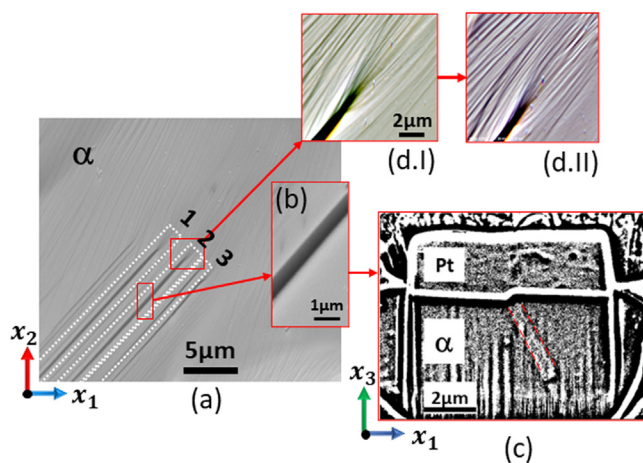


**Fig. 8.** An array of  $[11\bar{1}](112)$  slip bands within a ferrite grain; (a) SEM image with (b) zoomed image of slip band no. 2; (c) Contrast-enhanced image of FIB-sliced trench wall, at the location marked with red-square in a and magnified in b, to show the slip-plane (highlighted with dashed red lines). A Niblack local threshold [121] was applied to the in-lens secondary electron detector image to increase the image contrast of the slip band on the FIB trench surface (Pt is deposited platinum, and the vertical lines are FIB artefacts). (d) SEM image of the tip of slip band no.2 at applied displacements of (I) 1.1 mm and (II) 1.25 mm.

### 3.3. Loading of a slip band

The effect of the change of load on a ferrite slip band that terminated mid-grain was investigated by *in situ* observation. The slip band crossed a low-angle grain boundary (dashed white line Fig. 10a), and the slip band trace coincides with the (112) plane inclined by  $42 \pm 1^\circ$  to the surface ( $\theta$  in Fig. 1). A secondary slip band with the trace of (011) was also present in the field of view (Fig. 10a.ii). Using the local loading direction matrix (as in section 2.3), the  $[11\bar{1}](112)$  slip system has the highest Schmid factor, followed by  $[11\bar{1}](011)$  (see supplementary information B). The inclination angle ( $\psi$ ) of the shear direction in the  $[11\bar{1}](112)$  slip system is  $172.3 \pm 2.7^\circ$  (i.e., the Burgers vector lies almost parallel to the observed surface). The ‘bloom’ of diffuse contrast variation at the slip band tip increased in size as the applied loading was increased by the sample displacement (Fig. 10a), but there was no measurable change in the slip band thickness (i.e., no measurable change in height), which was constant at  $0.21 \mu\text{m}$ . The total GND density, estimated using the average within the cropped field of view of Fig. 10d that included the dislocations of the slip band, increased slightly with the applied displacement and was  $11.96 \pm 0.03 \log(\text{m}^{-2})$  at 1 mm and  $12.15 \pm 0.02 \log(\text{m}^{-2})$  at 1.2 mm.

Due to the proximity of the austenite-ferrite phase boundary, the  $J$ -integral analysis was constrained to 13 contours at 0.75 nm

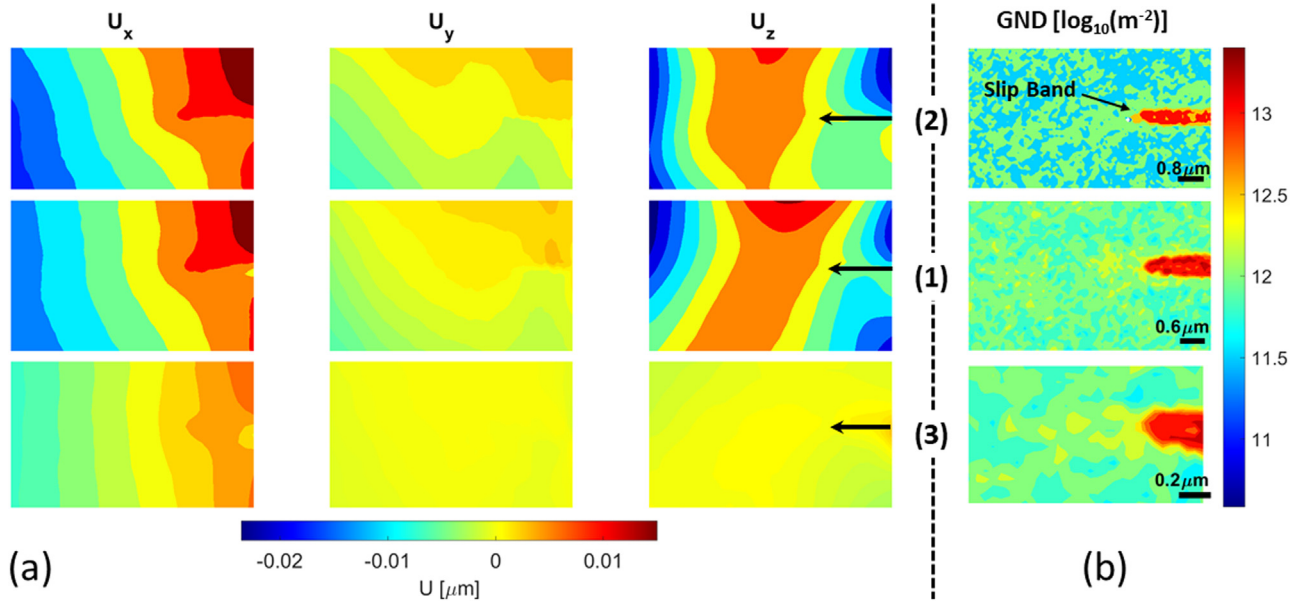


Fig. 9. (a) integrated elastic displacement fields for the  $[1\bar{1}\bar{1}](\bar{1}12)$  slip bands (labelled 1, 2 and 3); (b) GND density for the same slip bands.

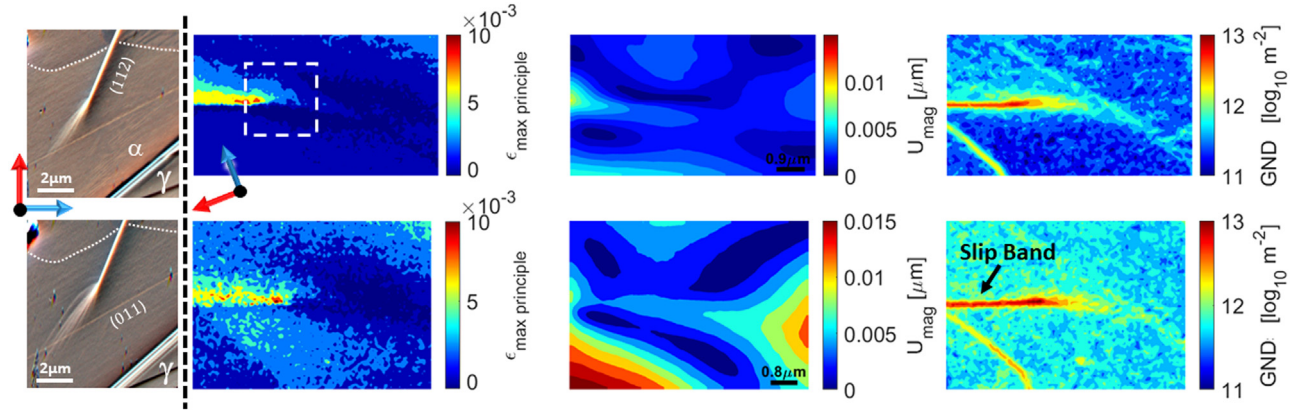


Fig. 10. *In situ* loading of a  $[1\bar{1}\bar{1}](112)$  slip band in a ferrite (a) grain using (a) VFSD imaging; (b) maximum principal strain; (c) integrated displacement magnitude; (d) GND density. The notation (i) and (ii) indicate observations with (i) 1 mm and (ii) 1.2 mm extension.

Table 3

Field parameters calculated for the  $[1\bar{1}\bar{1}](211)$  Slip bands array when the (nominal) extension was increased from 1 to 1.2 mm extension. The in-plane mode I is noted as  $K_I$  and the symmetrical out-of-plane contribution to mode I as  $K_I^T$ . The total mode I ( $K_I^T$  in Eq. (15)) is the summation of the in-plane mode I ( $K_I$ ) and  $K_I^T$ . The negative sign of the in-plane  $K_{II}$  and out-of-plane  $K_{III}$  shear depends on the arrangement of the nodes at the tip and does not carry any physical meaning. Full convergence is shown in Supplementary Information A.

Extension (mm)	$J$ (J m <sup>-2</sup> )	$K_I$ (MPa m <sup>0.5</sup> )	$K_{II}$ (MPa m <sup>0.5</sup> )	$K_{III}$ (MPa m <sup>0.5</sup> )	$K_I^T$ (MPa m <sup>0.5</sup> )	$K_I^T$ (MPa m <sup>0.5</sup> )	GND density (log <sub>10</sub> m <sup>-2</sup> )
1	0.55 ± 0.02	-0.17 ± 0.00	0.30 ± 0.01	0.02 ± 0.00	0.02 ± 0.01	-0.15 ± 0.01	11.96 ± 0.03
1.2	1.67 ± 0.03	0.14 ± 0.06	0.59 ± 0.01	-0.02 ± 0.01	0.01 ± 0.00	0.15 ± 0.07	12.15 ± 0.02

intervals ( $\sim 2 \times 2 \mu\text{m}^2$  region highlighted with the dashed white box in Fig. 10b with the slip band tip at the centre). Convergence was achieved after the 6<sup>th</sup> contour (0.68  $\mu\text{m}$  away from the slip band tip), with average value and variance taken from the 9<sup>th</sup> to 13<sup>th</sup> contours. The results (Table 3) show that the  $J$ -integral and mode I and mode II stress intensity factors increased as the specimen displacement was increased (i.e., increasing load). The mode II stress intensity factor was most significant. The mode III stress intensity factor and its additional contribution  $K_I^T$  to the mode I stress intensity factor were negligible.

This analysis of the effect of loading observed a slip band in a grain where the slip system of the highest Schmid factor had a Burgers vector at  $172.3^\circ$  to the surface (i.e., very close to the surface). This direction would favour in-plane shear with very little

out-of-plane shear. Therefore, the slip band responded to load with no measurable change in the observed width of the slip band, as there was no significant change in its height. The mode III stress intensity factor is low due to the negligible out-of-plane shear and did not increase measurably with the applied load. The in-plane mode II stress field increased significantly with loading. The mode I stress intensity factor is judged to arise from the constraint of the local mode II plastic deformation of the slip band tip and increased with the applied load.

### 3.4. General discussion

The stress field measured at the slip-band tip is due to the three-dimensional deformation that occurs as the concentrated

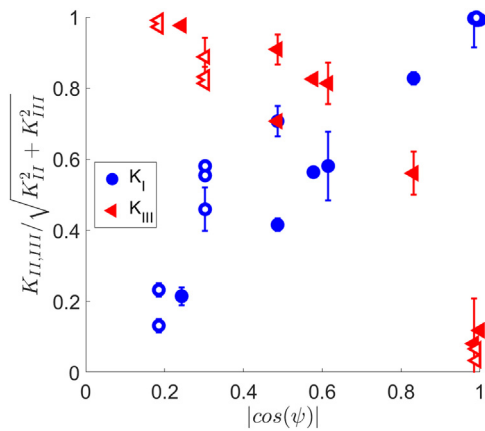


**Fig. 11.** The relationship of the mechanical conditions at the slip band tip to the slip inclination angle ( $\psi$ ). Mode II and III contributions are presented relative to the magnitude of the effective shear stress intensity factor ( $\sqrt{K_{II}^2 + K_{III}^2}$ ). Data from the exemplars in the main text are presented as open symbols. The additional data points from *in situ* studies of other slip bands are described in supplementary information A and are presented with solid symbols.

plastic shear of the slip band locally stretches the surrounding surface membrane. Here, the 3D elastic field has been quantified by (HR) EBSD, leading to its parameterisation by mode I, II and III stress intensity factors. It is important to recognise that the elastic mode I stress intensity factor does not arise from any opening displacement (i.e., volume change) of the slip band since this cannot occur for dislocation glide. The mode I stress intensity factor is from the tensile stretching that accommodates the height change of the surface membrane due to the mode III shear, as it is constrained by the surrounding matrix [118]. Mode II plastic shear would similarly interact with the mode I field, and the constrained deformation would also affect the stress intensity factors in mode II and III. Hence, the surface characterisation by (HR)-EBSD does not accurately describe the stress field that would exist in a slip band embedded within a 3-dimensional assembly of grains.

Nonetheless, the current elastic analysis provides a quantitative measure that may be useful in interpreting slip band behaviour and interactions with other microstructure features. In-plane and out-of-plane deformations have previously been observed, but could not be quantified, in a study that used digital image correlation of secondary electron images to examine the apparent strain concentrations of persistent slip bands that initiated fatigue cracks [118]. That analysis only provided the total strains on the surface (i.e., no elastic strain measurement), but the two-dimensional measurements found a relationship between the in-plane shear and tensile strains, which depended on the inclination angle of shear direction relative to the surface trace (i.e.,  $\psi$ ). Slip systems with in-plane shear (slight inclination angle,  $\psi$ ) gave small tensile strains due to the lack of out-of-plane deformation, whereas out-of-plane shear (larger inclination angle,  $\psi$ , approaching 90°) shows more significant tensile strains relative to the shear strains.

The relationship between the shear direction in the slip plane, measured by the slip inclination angle ( $\psi$ ), and the shear modes II and III of the stress intensity factors, measured via (HR)-EBSD in this work, is presented in Fig. 11. This plot includes data from the three exemplar studies above and additional *in situ* observations analysed similarly (see supplementary information A). Fig. 11 shows that mode II dominates at slip inclination angles closer to 0° or 180°, whereas mode III dominates near 90°. The mode ratio shows a clear trend with the slip inclination angle. The minor deviations from this trend may be attributed to variations in the slip plane orientation ( $\theta$ ) with respect to the surface, which

would be a secondary effect in these data due to its more limited range.

The observations may provide some insight into the propagation of slip bands. These terminate or arrest due to the interaction of their emitted dislocations [122] with the surrounding crystal and interfaces such as grain boundaries. Du et al. [123] showed that the visible slip traces at the surface are due to dislocation loops meeting the surface; the step acts as a stress relaxing mechanism [123–125]. Slip bands are sites where the shear deformation by mobile dislocations is localised rather than diffuse. Diffuse plastic deformation at the slip band tip acts to relax the stress field [122,126] as the matrix yields [127], which would affect the measured stress fields. The change in surface topology from diffuse plastic deformation is observed as the ‘bloom’ contrast (Fig. 9a). Due to this plastic deformation, the total in-plane and out-of-plane displacements are more significant than the elastic displacements (Fig. 10c) that cause the stress field. The intensity of this topographical blooming and the elastic displacement magnitude increased with loading (Fig. 10a) and slip band step height (Fig. 8a), but it was not directly linked to high GND density.

The elastic deformation field measured ahead of the slip band describes the stresses in the surface membrane of the observed grain. These are due to the plastic deformation at the tip of the slip band. The localisation of plastic deformation in the slip band is analogous to a mode II/III crack tip opening displacement, as the displacement is a shear that occurs only in a direction within the plane of the slip band. As noted above, this displacement is accommodated by diffuse plastic deformation (the observed ‘bloom’), and the elastic field is, therefore, similar to the HRR singularity in the plastic zone of a crack [128,129]. The slip system that defines the slip band is the slip system of the highest Schmid factor due to the local stress tensor acting in the grain, which arises from the applied loading and interactions with adjacent grains. The Burgers vector of this slip system defines the direction of plastic shear in the slip band ( $\psi$  in Fig. 1). For shear directions with an inclination angle that is not close to the surface plane (i.e.,  $|\cos \psi| \gg 0$ ), the slip band height increases as the magnitude of the shear increases. Hence, there is an increase in the magnitude of the elastic mode II and III stress intensity factors in the general case with increasing slip band height (Table 2). In the case where the Burgers vector is almost normal to the observed grain surface (Fig. 7, i.e. (i.e.  $|\cos \psi| \sim 1$ )), the stress field is mostly mode III, and in the case where the shear is almost parallel to the surface (Fig. 10), the stress field is mostly mode II (i.e.,  $|\cos \psi| \sim 0$ ). This leads to the general trend of the ratio of mode II to mode III stress intensity factors with the slip inclination angle (Fig. 11).

Therefore, there is a direct connection between the calculated stress intensity factors and the mechanical conditions at the tip of the slip band. The stress field is affected by relaxation from plastic deformation close to the slip band tip and the constrained changes in the surface topography due to the out-of-plane shear of the slip band. However, the quantitative analysis of the stress fields shows they are sensitive to the mode and magnitude of deformation of the slip band.

The (HR)-EBSD technique provides a combination of sensitivity, spatial resolution, and ease of use compared to other techniques [130–132] used to study elastic and plastic deformation. It provides an alternative to micro-mechanical experiments with pillars and cantilevers, which have drawbacks that include the adverse effect of FIB milling preparation, including inducing residual stress and embrittlement [133], pre-strain [134], length-scale dependency [135], and the different behaviour between constrained and unconstrained crystals [136]. The (HR)-EBSD analysis method to parameterise stress concentrations described here improves the in-plane method previously used to explore twinning [137] as it extends the analysis to the third dimension. It does, however, re-



quire an approximate estimate of the depth resolution EBSPs', and this might affect the reliability of the evaluation of the magnitudes of  $K_{III}$  and  $K_I^r$  (see supplementary information E). This analysis method may be valuable for examining the local conditions that control short fatigue crack propagation. A direct and quantitative assessment would be possible of the modes and magnitudes of the 3D elastic fields connected to the local plastic deformations at the crack tip, as these control its propagation [138–141].

Some factors lead to quantitative limitations in the current analysis. For instance, the current method of selecting the least deformed pattern as a reference may still suffer from 'the reference pattern problem' [82,142], which would be affected by the background stress due to the remote load and, to a lesser extent, by residual stresses from differential thermal contraction of ferrite and austenite (e.g., [143]). This minimally affects the GND density but does affect the magnitude of the strain component. Consequently, an incorrect reference would lead to errors in the magnitudes of the calculated  $J$ -integral and decomposed stress intensity factors in the integrated displacement field. An absolute three-dimensional lattice strain field can be obtained using micro-Laue microdiffraction [144–146] and dark-field X-ray microscopy [147], and future studies may employ such techniques. Experimental measurements [148,149] have shown that (HR)-EBSD is inaccurate in estimating the distribution or magnitude of the out-of-plane shear strain components, which will affect the reliability of the integrated  $U_z$  and consequently  $K_{III}$  and  $K_I^r$ . The integrated out-of-plane displacement ( $U_z$ ) is also affected by the size of the selected window for integration (see supplementary information E). This will directly affect  $K_{III}$ , with an effect also on mode I through the symmetrical out-of-plane field (i.e.,  $K_I^r$ ). However, it does not affect the in-plane displacement components ( $U_x$  and  $U_y$ ). Finally, to a lesser extent, the assumption of a traction-free surface ( $\sigma_{33} = 0$ ) that is conventionally made for (HR)-EBSD analysis might not be entirely accurate for the loaded slip band due to image forces at the free surface [150]. However, a counter-argument can be made by considering the small depth of information ( $<200$  nm) [151]. Most of these limitations would apply to any assessment by (HR)-EBSD of the surface stress fields since they are affected by the out-of-plane deformations, and the limitation is not specific to their parameterisation as stress intensity factors.

#### 4. Conclusion

Slip bands that were terminated mid-grain in the ferrite phase of a 475 °C age-hardened duplex stainless-steel (Zeron 100: 25%Cr, 7%Ni) have been characterised *in situ* using electron backscatter diffraction (EBSD), high (angular) resolution (HR)-EBSD and secondary electron (SE) imaging. A novel analysis used the measured stress field to determine the local Schmid factors of the slip systems in the observed grains; this was validated by observing the slip band plane and shear direction.

The local measurements allowed a novel 3D parametrisation of the stress fields at the slip band tip by evaluating the potential elastic strain energy release rate ( $J$ -integral). This was decomposed using auxiliary fields, with the assumption of small-scale plasticity, to obtain the three-dimensional stress intensity factors that described the magnitudes and modes of the stress concentration. The analysis was demonstrated by examining the mechanical conditions at an incipient slip band, the direct effect of the slip band height in an array of parallel slip bands, and the effect of loading of a slip band. The three-dimensional stress intensity factors were consistent with the magnitude and mode of the shear of the slip band; the ratio of the mode II to mode III stress intensity factors depended on the slip inclination angle relative to the observed surface.

The constraint of the topological changes of the surface due to shear induces additional tensile stresses; hence, the surface analysis does not provide an absolute measure of the modes of stress concentration of the slip band that would occur within a three-dimensional polycrystal. Nonetheless, this analysis provides a quantitative description of the stress fields of slip bands that affect their interaction with microstructure. Future applications are identified for other important stress concentrating features such as short fatigue cracks.

#### Declaration of Competing Interest

The authors declare that they have no known competing financial interests or personal relationships that could have appeared to influence the work reported in this paper.

#### CRediT authorship contribution statement

**Abd alrhman Koko:** Methodology, Software, Investigation, Formal analysis, Writing – original draft, Visualization. **Elsiddig Elmukashfi:** Writing – review & editing. **Thorsten H. Becker:** Methodology. **Phani S. Karamched:** Formal analysis. **Angus J. Wilkinson:** Software. **T. James Marrow:** Visualization, Resources, Writing – review & editing, Supervision, Funding acquisition.

#### Acknowledgements

We thank Dr Roger Francis (Rolled Alloys [www.rolledalloys.com](http://www.rolledalloys.com)) for supplying the specimen material, Dr Kalin Dragnevski and Ms Marzena Tkaczyk (Laboratory for *In-situ* Microscopy and Analysis, LIMA) for support with the experiment, and Mr Marin Vukšić and Mr Marcus Williamson (Materials, University of Oxford) for help with Focused Ion Beam (FIB) milling and TEM. The authors acknowledge the use of characterisation facilities within the David Cockayne Centre for Electron Microscopy (DCEM), Department of Materials, University of Oxford, alongside financial support provided by the Henry Royce Institute (Grant ref EP/R010145/1). Abd alrhman Koko is supported by an EPSRC research studentship (Grant ref EP/N509711/1).

#### Supplementary materials

Supplementary material associated with this article can be found, in the online version, at doi:[10.1016/j.actamat.2022.118284](https://doi.org/10.1016/j.actamat.2022.118284).

#### References

- [1] J.H. Panchal, S.R. Kalidindi, D.L. McDowell, Key computational modeling issues in integrated computational materials engineering, *Comput. Aided Des.* 45 (2013) 4–25, doi:[10.1016/j.cad.2012.06.006](https://doi.org/10.1016/j.cad.2012.06.006).
- [2] B. Chen, J. Jiang, F.P.E. Dunne, Microstructurally-sensitive fatigue crack nucleation in Ni-based single and oligo crystals, *J. Mech. Phys. Solids* 106 (2017) 15–33, doi:[10.1016/j.jmps.2017.05.012](https://doi.org/10.1016/j.jmps.2017.05.012).
- [3] D.L. McDowell, F.P.E. Dunne, Microstructure-sensitive computational modeling of fatigue crack formation, *Int. J. Fatigue* 32 (2010) 1521–1542, doi:[10.1016/j.ijfatigue.2010.01.003](https://doi.org/10.1016/j.ijfatigue.2010.01.003).
- [4] D. Wilson, Z. Zheng, F.P.E. Dunne, A microstructure-sensitive driving force for crack growth, *J. Mech. Phys. Solids* 121 (2018) 147–174, doi:[10.1016/j.jmps.2018.07.005](https://doi.org/10.1016/j.jmps.2018.07.005).
- [5] N. Grilli, A.C.F. Cocks, E. Tarleton, A phase field model for the growth and characteristic thickness of deformation-induced twins, *J. Mech. Phys. Solids* 143 (2020) 104061, doi:[10.1016/j.jmps.2020.104061](https://doi.org/10.1016/j.jmps.2020.104061).
- [6] R. Pokharel, J. Lind, A.K. Kanjarla, R.A. Lebensohn, S.F. Li, P. Kenesei, et al., Polycrystal plasticity: comparison between grain - scale observations of deformation and simulations, *Annu. Rev. Condens. Matter Phys.* 5 (2014) 317–346, doi:[10.1146/annurev-conmatphys-031113-133846](https://doi.org/10.1146/annurev-conmatphys-031113-133846).
- [7] D. Chandrasekaran, M. Nygård, A study of the surface deformation behaviour at grain boundaries in an ultra-low-carbon steel, *Acta Mater.* 51 (2003) 5375–5384, doi:[10.1016/S1359-6454\(03\)00394-X](https://doi.org/10.1016/S1359-6454(03)00394-X).
- [8] M. Zhang, F. Bridier, P. Villechaise, J. Mendez, D.L. McDowell, Simulation of slip band evolution in duplex Ti–6Al–4V, *Acta Mater.* 58 (2010) 1087–1096, doi:[10.1016/j.actamat.2009.10.025](https://doi.org/10.1016/j.actamat.2009.10.025).

- [9] F.P.E. Dunne, Fatigue crack nucleation: mechanistic modelling across the length scales, *Curr. Opin. Solid State Mater. Sci.* 18 (2014) 170–179, doi:[10.1016/j.cossms.2014.02.005](https://doi.org/10.1016/j.cossms.2014.02.005).
- [10] Y. Wang, J. Li, Phase field modeling of defects and deformation, *Acta Mater.* 58 (2010) 1212–1235, doi:[10.1016/j.actamat.2009.10.041](https://doi.org/10.1016/j.actamat.2009.10.041).
- [11] M. Fleck, F. Querfurth, U. Glatzel, Phase field modeling of solidification in multi-component alloys with a case study on the Inconel 718 alloy, *J. Mater. Res.* 32 (2017) 4605–4615, doi:[10.1557/jmr.2017.393](https://doi.org/10.1557/jmr.2017.393).
- [12] T.B. Britton, A.J. Wilkinson, Stress fields and geometrically necessary dislocation density distributions near the head of a blocked slip band, *Acta Mater.* 60 (2012) 5773–5782, doi:[10.1016/j.actamat.2012.07.004](https://doi.org/10.1016/j.actamat.2012.07.004).
- [13] Y. Guo, T.B. Britton, A.J. Wilkinson, Slip band–grain boundary interactions in commercial-purity titanium, *Acta Mater.* 76 (2014) 1–12, doi:[10.1016/j.actamat.2014.05.015](https://doi.org/10.1016/j.actamat.2014.05.015).
- [14] M.T. Andani, A. Lakshmanan, V. Sundaragharavan, J. Allison, A. Misra, Quantitative study of the effect of grain boundary parameters on the slip system level Hall–Petch slope for basal slip system in Mg–4Al, *Acta Mater.* 200 (2020) 148–161, doi:[10.1016/j.actamat.2020.08.079](https://doi.org/10.1016/j.actamat.2020.08.079).
- [15] J.D. Livingston, B. Chalmers, Multiple slip in bicrystal deformation, *Acta Metall.* 5 (1957) 322–327, doi:[10.1016/j.actamat.2012.07.004](https://doi.org/10.1016/j.actamat.2012.07.004).
- [16] T.C. Lee, I.M. Robertson, H.K. Birnbaum, Prediction of slip transfer mechanisms across grain boundaries, *Scr. Metall.* 23 (1989) 799–803, doi:[10.1016/0036-9748\(89\)90534-6](https://doi.org/10.1016/0036-9748(89)90534-6).
- [17] J. Luster, M.A. Morris, Compatibility of deformation in two-phase Ti–Al alloys: dependence on microstructure and orientation relationships, *Metall. Mater. Trans. A* 26 (1995) 1745–1756, doi:[10.1007/BF02670762](https://doi.org/10.1007/BF02670762).
- [18] D.A. Koss, K.S. Chan, Fracture along planar slip bands, *Acta Metall.* 28 (1980) 1245–1252, doi:[10.1016/0001-6160\(80\)90080-2](https://doi.org/10.1016/0001-6160(80)90080-2).
- [19] H. Mughrabi, Dislocation wall and cell structures and long-range internal stresses in deformed metal crystals, *Acta Metall.* 31 (1983) 1367–1379, doi:[10.1016/0001-6160\(83\)90007-X](https://doi.org/10.1016/0001-6160(83)90007-X).
- [20] P. Lukáš, M. Klesnil, J. Krejčí, Dislocations and persistent slip bands in copper single crystals fatigued at low stress amplitude, *Physica Status Solidi (b)* 27 (1968) 545–558, doi:[10.1002/psbb.19680270212](https://doi.org/10.1002/psbb.19680270212).
- [21] S.T. Tu, X.C. Zhang, Fatigue crack initiation mechanisms, Reference Module in Materials Science and Materials Engineering, Elsevier, 2016, doi:[10.1016/B978-0-12-803581-8.02852-6](https://doi.org/10.1016/B978-0-12-803581-8.02852-6).
- [22] J.R. Rice, Tensile crack tip fields in elastic-ideally plastic crystals, *Mech. Mater.* 6 (1987) 317–335, doi:[10.1016/0167-6636\(87\)90030-5](https://doi.org/10.1016/0167-6636(87)90030-5).
- [23] Makin M.J. The mechanism of slip band growth in irradiated crystals. 101080/14786437008238467 2006;21:815–7. 10.1080/14786437008238467.
- [24] J.K. Knowles, E. Sternberg, On a class of conservation laws in linearized and finite elastostatics, *Arch. Ration. Mech. Anal.* 44 (1972) 187–211, doi:[10.1007/BF00250778](https://doi.org/10.1007/BF00250778).
- [25] E. Noether, Invariant variation problems, *Transp. Theory Stat. Phys.* 1 (1971) 186–207, doi:[10.1080/00411457108231446](https://doi.org/10.1080/00411457108231446).
- [26] B. Budiansky, J.R. Rice, Conservation laws and energy-release rates, *J. Appl. Mech.* 40 (1973) 201–203, doi:[10.1115/1.3422926](https://doi.org/10.1115/1.3422926).
- [27] J.D. Eshelby, The force on an elastic singularity, *Philos. Trans. R. Soc. Lond. Ser. A Math. Phys. Sci.* 244 (1951) 87–112, doi:[10.1098/rsta.1951.0016](https://doi.org/10.1098/rsta.1951.0016).
- [28] R. Kienzler, G. Herrmann, *Mechanics in Material Space: With Applications to Defect and Fracture Mechanics*, Springer Science & Business Media, Berlin, Germany, 2000.
- [29] G.A. Maugin, *Configurational Forces: Thermomechanics, Physics, Mathematics, and Numerics*, CRC Press/Taylor & Francis, Boca Raton, Florida, 2011.
- [30] E. Agiasofitou, M. Lazar, Micromechanics of dislocations in solids: J-, M-, and L-integrals and their fundamental relations, *Int. J. Eng. Sci.* 114 (2017) 16–40, doi:[10.1016/j.iengsci.2017.02.001](https://doi.org/10.1016/j.iengsci.2017.02.001).
- [31] H. Kim, S. Kim, S.Y. Kim, Lattice-based J integral for a steadily moving dislocation, *Int. J. Plast.* 138 (2021) 102949, doi:[10.1016/j.ijplas.2021.102949](https://doi.org/10.1016/j.ijplas.2021.102949).
- [32] X. Markenscoff, L. Ni, The energy-release rate and “self-force” of dynamically expanding spherical and plane inclusion boundaries with dilatational eigenstrain, *J. Mech. Phys. Solids* 58 (2010) 1–11, doi:[10.1016/j.jmps.2009.10.001](https://doi.org/10.1016/j.jmps.2009.10.001).
- [33] J. Rice, W. Drugan, T.L. Sham, in: *Elastic-Plastic Analysis of Growing Cracks*, Fracture Mechanics, ASTM International, West Conshohocken, 1979, pp. 33–189, doi:[10.1520/STP36972S](https://doi.org/10.1520/STP36972S). 100 Barr Harbor Drive, PO Box C700PA 19428-2959.
- [34] A.C. Palmer, J.R. Rice, R. Hill, The growth of slip surfaces in the progressive failure of over-consolidated clay, *Proc. R. Soc. Lond. A Math. Phys. Sci.* 332 (1973) 527–548, doi:[10.1098/rspa.1973.0040](https://doi.org/10.1098/rspa.1973.0040).
- [35] J.R. Rice, Dislocation nucleation from a crack tip: an analysis based on the Peierls concept, *J. Mech. Phys. Solids* 40 (1992) 239–271, doi:[10.1016/S0022-5096\(05\)80012-2](https://doi.org/10.1016/S0022-5096(05)80012-2).
- [36] K.C. Amit, J.H. Kim, Interaction integrals for thermal fracture of functionally graded materials, *Eng. Fract. Mech.* 75 (2008) 2542–2565, doi:[10.1016/j.engfractmech.2007.07.011](https://doi.org/10.1016/j.engfractmech.2007.07.011).
- [37] H. Haftbaradaran, J. Qu, A path-independent integral for fracture of solids under combined electrochemical and mechanical loadings, *J. Mech. Phys. Solids* 71 (2014) 1–14, doi:[10.1016/j.jmps.2014.06.007](https://doi.org/10.1016/j.jmps.2014.06.007).
- [38] M.C. Walters, G.H. Paulino, R.H. Dodds, Interaction integral procedures for 3-D curved cracks including surface tractions, *Eng. Fract. Mech.* 72 (2005) 1635–1663, doi:[10.1016/j.engfractmech.2005.01.002](https://doi.org/10.1016/j.engfractmech.2005.01.002).
- [39] T.H. Becker, M. Mostafavi, R.B. Tait, T.J. Marrow, An approach to calculate the J-integral by digital image correlation displacement field measurement, *Fatigue Fract. Eng. Mater. Struct.* 35 (2012) 971–984, doi:[10.1111/j.1460-2695.2012.01685.x](https://doi.org/10.1111/j.1460-2695.2012.01685.x).
- [40] S.M. Barhli, M. Mostafavi, A.F. Cinar, D. Hollis, T.J. Marrow, J-integral calculation by finite element processing of measured full-field surface displacements, *Exp. Mech.* 57 (2017) 997–1009, doi:[10.1007/s11340-017-0275-1](https://doi.org/10.1007/s11340-017-0275-1).
- [41] S.M. Barhli, L. Saucedo-Mora, C. Simpson, T. Becker, M. Mostafavi, P.J. Withers, et al., Obtaining the J-integral by diffraction-based crack-field strain mapping, *Procedia Struct. Integr.* 2 (2016) 2519–2526, doi:[10.1016/j.prostr.2016.06.315](https://doi.org/10.1016/j.prostr.2016.06.315).
- [42] S.M. Barhli, L. Saucedo-Mora, M.S.L. Jordan, A.F. Cinar, C. Reinhard, M. Mostafavi, et al., Synchrotron X-ray characterization of crack strain fields in polygranular graphite, *Carbon* 124 (2017) 357–371 N Y, doi:[10.1016/j.carbon.2017.08.075](https://doi.org/10.1016/j.carbon.2017.08.075).
- [43] A. Koko, P. Earp, T. Wigger, J. Tong, T.J. Marrow, J-integral analysis: An EDXD and DIC comparative study for a fatigue crack, *Int. J. Fatigue* 134 (2020) 105474, doi:[10.1016/j.ijfatigue.2020.105474](https://doi.org/10.1016/j.ijfatigue.2020.105474).
- [44] J.D. Eshelby, F. Seitz, D.B.T. Turnbull, The continuum theory of lattice defects, in: *Solid State Physics*, 3, Academic Press, 1956, pp. 79–144, doi:[10.1016/S0081-1947\(08\)60132-0](https://doi.org/10.1016/S0081-1947(08)60132-0). editors.
- [45] P.M. Anderson, J.P. Hirth, J. Lothe, *Theory of straight dislocations*, in: *Theory of Dislocations*, 3rd ed., Cambridge University Press, New York, 2017, pp. 85–89.
- [46] E. Agiasofitou, M. Lazar, A new insight into the J-, M-, and L-integrals of dislocations, *PAMM* 18 (2018) e201800159, doi:[10.1002/PAMM.201800159](https://doi.org/10.1002/PAMM.201800159).
- [47] J.D. Eshelby, J.M. Ball, D. Kinderlehrer, P. Podio-Guidugli, M. Slemrod, Energy relations and the energy-momentum tensor in continuum mechanics, in: *Fundamental Contributions to the Continuum Theory of Evolving Phase Interfaces in Solids*, Springer Berlin Heidelberg, Berlin, Heidelberg, 1999, pp. 82–119, doi:[10.1007/978-3-642-59938-5\\_5](https://doi.org/10.1007/978-3-642-59938-5_5).
- [48] M.X. Shi, Y. Huang, H. Gao, The J-integral and geometrically necessary dislocations in nonuniform plastic deformation, *Int. J. Plast.* 20 (2004) 1739–1762, doi:[10.1016/j.ijplas.2003.11.013](https://doi.org/10.1016/j.ijplas.2003.11.013).
- [49] Y.H. Chen, *Advances in Conservation Laws and Energy Release Rates*, Springer Netherlands, Dordrecht, 2002, doi:[10.1007/978-94-015-9908-5](https://doi.org/10.1007/978-94-015-9908-5).
- [50] M.A. Hussain, S.L. Pu, J. Underwood, G.R. Irwin, Strain energy release rate for a crack under combined mode I and mode II, in: *Fracture Analysis: Proceedings of the 1973 National Symposium on Fracture Mechanics, Part II*, ASTM International, West Conshohocken, 1974, pp. 2–28, doi:[10.1520/STP33130S](https://doi.org/10.1520/STP33130S). PA:.
- [51] A. Golebiewska Herrmann, G. Herrmann, On energy-release rates for a plane crack, *J. Appl. Mech.* 48 (1981) 525–528, doi:[10.1115/1.3157667](https://doi.org/10.1115/1.3157667).
- [52] J.H. Park, Y.Y. Earmme, Application of conservation integrals to interfacial crack problems, *Mech. Mater.* 5 (1986) 261–276, doi:[10.1016/0167-6636\(86\)90023-2](https://doi.org/10.1016/0167-6636(86)90023-2).
- [53] Y.H. Chen, T.J. Lu, Recent developments and applications of invariant integrals, *Appl. Mech. Rev.* 56 (2003) 515–552, doi:[10.1115/1.1582199](https://doi.org/10.1115/1.1582199).
- [54] T. Nishioka, S.N. Atluri, On the computation of mixed-mode K-factors for a dynamically propagating crack, using path-independent integrals J/K, *Eng. Fract. Mech.* 20 (1984) 193–208, doi:[10.1016/0013-7944\(84\)90128-0](https://doi.org/10.1016/0013-7944(84)90128-0).
- [55] F.Z. Li, C.F. Shih, A. Needleman, A comparison of methods for calculating energy release rates, *Eng. Fract. Mech.* 21 (1985) 405–421, doi:[10.1016/0013-7944\(85\)90029-3](https://doi.org/10.1016/0013-7944(85)90029-3).
- [56] G.P. Nikishkov, S.N. Atluri, Calculation of fracture mechanics parameters for an arbitrary three-dimensional crack, by the “equivalent domain integral” method, *Int. J. Numer. Methods Eng.* 24 (1987) 1801–1821, doi:[10.1002/nme.1620240914](https://doi.org/10.1002/nme.1620240914).
- [57] C.F. Shih, B. Moran, T. Nakamura, Energy release rate along a three-dimensional crack front in a thermally stressed body, *Int. J. Fract.* 30 (1986) 79–102, doi:[10.1007/BF00034019](https://doi.org/10.1007/BF00034019).
- [58] C.F. Shih, R.J. Asaro, Elastic-plastic analysis of cracks on bimaterial interfaces: part I – small scale yielding, *J. Appl. Mech.* 55 (1988) 299–316, doi:[10.1115/1.3173676](https://doi.org/10.1115/1.3173676).
- [59] H.A. Richard, B. Schramm, N.H. Schirmeisen, Cracks on mixed mode loading – theories, experiments, simulations, *Int. J. Fatigue* 62 (2014) 93–103, doi:[10.1016/j.fatigue.2013.06.019](https://doi.org/10.1016/j.fatigue.2013.06.019).
- [60] D.M. Parks, The virtual crack extension method for nonlinear material behavior, *Comput. Meth. Appl. Mech. Eng.* 12 (1977) 353–364, doi:[10.1016/0045-7825\(77\)90023-8](https://doi.org/10.1016/0045-7825(77)90023-8).
- [61] A. Koko, E. Elmukashfi, A.J. Wilkinson, T.J. Marrow, J-integral analysis of the strain fields of micro-cracks in single silicon crystal using HR-EBSD, in: *Proceedings of the 15th International Conference on Advances in Experimental Mechanics*, 2021.
- [62] C. Örneke, M.G. Burke, T. Hashimoto, D.L. Engelberg, 748 K (475°C) Embrittlement of duplex stainless steel: effect on microstructure and fracture behavior, *Metall. Mater. Trans. A* 48 (2017) 1653–1665, doi:[10.1007/s11661-016-3944-2](https://doi.org/10.1007/s11661-016-3944-2).
- [63] K.L. Weng, H.R. Chen, J.R. Yang, The low-temperature aging embrittlement in a 2205 duplex stainless steel, *Mater. Sci. Eng. A* 379 (2004) 119–132, doi:[10.1016/j.msea.2003.12.051](https://doi.org/10.1016/j.msea.2003.12.051).
- [64] O. Soriano-Vargas, E.O. Avila-Davila, V.M. Lopez-Hirata, N. Cayetano-Castro, J.L. Gonzalez-Velazquez, Effect of spinodal decomposition on the mechanical behavior of Fe–Cr alloys, *Mater. Sci. Eng. A* 527 (2010) 2910–2914, doi:[10.1016/j.msea.2010.01.020](https://doi.org/10.1016/j.msea.2010.01.020).
- [65] T.J. Marrow, A.O. Humphreys, M. Strangwood, The crack initiation toughness for brittle fracture of super duplex stainless steel, *Fatigue Fract. Eng. Mater. Struct.* 20 (1997) 1005–1014, doi:[10.1111/j.1460-2695.1997.tb01543.x](https://doi.org/10.1111/j.1460-2695.1997.tb01543.x).
- [66] S.I. Wright, M.M. Nowell, R. de Kloe, P. Camus, T. Rampton, Electron imaging with an EBSD detector, *Ultramicroscopy* 148 (2015) 132–145, doi:[10.1016/j.ultramic.2014.10.002](https://doi.org/10.1016/j.ultramic.2014.10.002).
- [67] A.J. Wilkinson, D. Randman, Determination of elastic strain fields and geometrically necessary dislocation distributions near nanoindentations using

- electron back scatter diffraction, *Philos. Mag.* 90 (2010) 1159–1177, doi:[10.1080/14786430903304145](https://doi.org/10.1080/14786430903304145).
- [68] J. Jiang, T.B. Britton, A.J. Wilkinson, Measurement of geometrically necessary dislocation density with high resolution electron backscatter diffraction: effects of detector binning and step size, *Ultramicroscopy* 125 (2013) 1–9, doi:[10.1016/j.ultramic.2012.11.003](https://doi.org/10.1016/j.ultramic.2012.11.003).
- [69] A.J. Wilkinson, Measurement of elastic strains and small lattice rotations using electron back scatter diffraction, *Ultramicroscopy* 62 (1996) 237–247, doi:[10.1016/0304-3991\(95\)00152-2](https://doi.org/10.1016/0304-3991(95)00152-2).
- [70] T.J. Ruggles, D.T. Fullwood, J.V. Kysar, Resolving geometrically necessary dislocation density onto individual dislocation types using EBSD-based continuum dislocation microscopy, *Int. J. Plast.* 76 (2016) 231–243, doi:[10.1016/j.jiplas.2015.08.005](https://doi.org/10.1016/j.jiplas.2015.08.005).
- [71] V. Randle, Theoretical framework for electron backscatter diffraction, in: A.J. Schwartz, M. Kumar, B.L. Adams (Eds.), *Electron Backscatter Diffraction in Materials Science*, 1st ed., Springer US, Boston, MA, 2000, pp. 19–30, doi:[10.1007/978-1-4757-3205-4\\_2](https://doi.org/10.1007/978-1-4757-3205-4_2).
- [72] S. Sawatzki, T.G. Woodcock, K. Güth, K.H. Müller, O. Gutfleisch, Calculation of remanence and degree of texture from EBSD orientation histograms and XRD rocking curves in Nd–Fe–B sintered magnets, *J. Magn. Magn. Mater.* 382 (2015) 219–224, doi:[10.1016/j.jmmm.2015.01.046](https://doi.org/10.1016/j.jmmm.2015.01.046).
- [73] S.I. Wright, M.M. Nowell, D.P. Field, A review of strain analysis using electron backscatter diffraction, *Microsc. Microanal.* 17 (2011) 316–329, doi:[10.1017/S1431927611000055](https://doi.org/10.1017/S1431927611000055).
- [74] K.Z. Troost, P. van der Sluis, D.J. Gravesteijn, Microscale elastic-strain determination by backscatter Kikuchi diffraction in the scanning electron microscope, *Appl. Phys. Lett.* 62 (1993) 1110–1112, doi:[10.1063/1.108758](https://doi.org/10.1063/1.108758).
- [75] A.J. Wilkinson, G. Meaden, D.J. Dingley, High resolution mapping of strains and rotations using electron backscatter diffraction, *Mater. Sci. Technol.* 22 (2006) 1271–1278, doi:[10.1179/174328406X130966](https://doi.org/10.1179/174328406X130966).
- [76] T.B. Britton, A.J. Wilkinson, Measurement of residual elastic strain and lattice rotations with high resolution electron backscatter diffraction, *Ultramicroscopy* 111 (2011) 1395–1404, doi:[10.1016/j.ultramic.2011.05.007](https://doi.org/10.1016/j.ultramic.2011.05.007).
- [77] A. Koko, A.J. Wilkinson, T.J. Marrow, An iterative method for reference pattern selection in high resolution electron backscatter diffraction (HR-EBSD), *Ultramicroscopy* (2022) (Under Review), doi:[10.48550/arXiv.2206.10242](https://doi.org/10.48550/arXiv.2206.10242).
- [78] F. Bachmann, R. Hielscher, H. Schaeben, Grain detection from 2d and 3d EBSD data – specification of the MTEX algorithm, *Ultramicroscopy* 111 (2011) 1720–1733, doi:[10.1016/j.ultramic.2011.08.002](https://doi.org/10.1016/j.ultramic.2011.08.002).
- [79] S. Zaefferer, On the formation mechanisms, spatial resolution and intensity of backscatter Kikuchi patterns, *Ultramicroscopy* 107 (2007) 254–266, doi:[10.1016/j.ultramic.2006.08.007](https://doi.org/10.1016/j.ultramic.2006.08.007).
- [80] T.B. Britton, V.S. Tong, J. Hickey, A. Foden, A.J. Wilkinson, AstroEBSD : exploring new space in pattern indexing with methods launched from an astronomical approach, *J. Appl. Crystallogr.* 51 (2018) 1525–1534, doi:[10.1107/S1600576718010373](https://doi.org/10.1107/S1600576718010373).
- [81] S. Weiss, U. Klement, Orientation determination on non planar surfaces, in: *Proceedings of the Channel Users Meeting*, Ribe, Denmark, 2004, pp. 9–11.
- [82] A.J. Wilkinson, B.T. Ben, Strains, planes, and EBSD in materials science, *Mater. Today* 15 (2012) 366–376, doi:[10.1016/S1369-7021\(12\)70163-3](https://doi.org/10.1016/S1369-7021(12)70163-3).
- [83] J.D. Lord, B. Roebuck, R. Morrell, T. Lube, 25 Year perspective aspects of strain and strength measurement in miniaturised testing for engineering metals and ceramics, *Mater. Sci. Technol.* 26 (2010) 127–148, doi:[10.1179/026708309X12584564052012](https://doi.org/10.1179/026708309X12584564052012).
- [84] A.J. Wilkinson, G. Meaden, D.J. Dingley, High-resolution elastic strain measurement from electron backscatter diffraction patterns: new levels of sensitivity, *Ultramicroscopy* 106 (2006) 307–313, doi:[10.1016/j.ultramic.2005.10.001](https://doi.org/10.1016/j.ultramic.2005.10.001).
- [85] S. Villert, C. Maurice, C. Wyon, R. Fortunier, Accuracy assessment of elastic strain measurement by EBSD, *J. Microsc.* 233 (2009) 290–301, doi:[10.1111/j.1365-2818.2009.03120.x](https://doi.org/10.1111/j.1365-2818.2009.03120.x).
- [86] F. Bachmann, R. Hielscher, H. Schaeben, Texture analysis with MTEX – free and open source software toolbox, *Solid State Phenomena* 160 (2010) 63–68, doi:[10.4028/www.scientific.net/SSP.160.63](https://doi.org/10.4028/www.scientific.net/SSP.160.63).
- [87] C.M. Cepeda-Jiménez, J.M. Molina-Aldareguia, M.T. Pérez-Prado, EBSD-assisted slip trace analysis during *in situ* SEM mechanical testing: application to unravel grain size effects on plasticity of pure Mg polycrystals, *JOM* 68 (2016) 116–126, doi:[10.1007/s11837-015-1521-6](https://doi.org/10.1007/s11837-015-1521-6).
- [88] Y.T. Tang, N. D'Souza, B. Roebuck, P. Karamched, C. Panwisawas, D.M. Collins, Ultra-high temperature deformation in a single crystal superalloy: mesoscale process simulation and micromechanisms, *Acta Mater.* 203 (2021) 116468, doi:[10.1016/j.actamat.2020.11.010](https://doi.org/10.1016/j.actamat.2020.11.010).
- [89] S.F. Bordin, S. Limandri, J.M. Ranailli, G. Castellano, EBSD spatial resolution for detecting sigma phase in steels, *Ultramicroscopy* 171 (2016) 177–185, doi:[10.1016/j.ultramic.2016.09.010](https://doi.org/10.1016/j.ultramic.2016.09.010).
- [90] P. Hovington, D. Drouin, R. Gauvin, CASINO: a new Monte Carlo code in C language for electron beam interaction – part I: description of the program, *Scanning* 19 (1997) 1–14, doi:[10.1002/sca.4950190101](https://doi.org/10.1002/sca.4950190101).
- [91] E. Schmidt-Rieder, M. Ashworth, J.P.G. Farr, The effect of nitrogen on the stability of the passive film on a zeron 100 super duplex stainless steel, *Electrochim. Solid State Lett.* 2 (1999) 19–21, doi:[10.1149/1.1390720/XML](https://doi.org/10.1149/1.1390720/XML).
- [92] Koko A., Marrow J., Elmukashfi E. A computational method for the determination of the elastic displacement field using measured elastic deformation field. To Appear 2021:5. 10.48550/arXiv.2107.10330.
- [93] M. Mostafavi, D.M. Collins, B. Cai, R. Bradley, R.C. Atwood, C. Reinhard, et al., Yield behavior beneath hardness indentations in ductile metals, measured by three-dimensional computed X-ray tomography and digital volume correlation, *Acta Mater.* 82 (2015) 468–482, doi:[10.1016/j.actamat.2014.08.046](https://doi.org/10.1016/j.actamat.2014.08.046).
- [94] Helm J.D., McNeill S.R., Sutton M.A. Improved three-dimensional image correlation for surface displacement measurement. 101117/1600624 1996;35, 1911–20. 10.1117/1.600624.
- [95] K.L. Chen, S.N. Atluri, Comparison of different methods of evaluation of weight functions for 2-D mixed-mode fracture analyses, *Eng. Fract. Mech.* 34 (1989) 935–956, doi:[10.1016/0013-7944\(89\)90230-0](https://doi.org/10.1016/0013-7944(89)90230-0).
- [96] T. Nishioka, S.N.N. Atluri, On the computation of mixed-mode for a dynamically propagating crack, using path-independent integrals, *Eng. Fract. Mech.* 20 (1984) 193–208, doi:[10.1016/0013-7944\(84\)90128-0](https://doi.org/10.1016/0013-7944(84)90128-0).
- [97] O. Huber, J. Nickel, G. Kuhn, On the decomposition of the *J*-integral for 3D crack problems, *Int. J. Fract.* 64 (1993) 339–348, doi:[10.1007/BF00017849](https://doi.org/10.1007/BF00017849).
- [98] K.N. Shivakumar, I.S. Raju, An equivalent domain integral method for three-dimensional mixed-mode fracture problems, *Eng. Fract. Mech.* 42 (1992) 935–959, doi:[10.1016/0013-7944\(92\)90134-Z](https://doi.org/10.1016/0013-7944(92)90134-Z).
- [99] R.H. Rigby, M.H. Aliabadi, Decomposition of the mixed-mode *J*-integral—revisited, *Int. J. Solids Struct.* 35 (1998) 2073–2099, doi:[10.1016/S0020-7683\(97\)00171-6](https://doi.org/10.1016/S0020-7683(97)00171-6).
- [100] S.S. Wang, J.F. Yau, Interfacial cracks in adhesively bonded scarf joints, *AIAA J.* 19 (1981) 1350–1356, doi:[10.2514/3.7865](https://doi.org/10.2514/3.7865).
- [101] M.R. Molteno, T.H. Becker, Mode I–III decomposition of the *J*-integral from DIC displacement data, *Strain* 51 (2015) 492–503, doi:[10.1111/str.12166](https://doi.org/10.1111/str.12166).
- [102] H. Ishikawa, H. Kitagawa, H. Okamura, *J* integral of a mixed mode crack and its application, *Mech. Behav. Mater.* 3 (1980) 447–455 Elsevier, doi:[10.1016/B978-1-4832-8414-9.50137-1](https://doi.org/10.1016/B978-1-4832-8414-9.50137-1).
- [103] S. Courtin, C. Gardin, G. Bézeine, H. ben Hadj Hamouda, Advantages of the *J*-integral approach for calculating stress intensity factors when using the commercial finite element software ABAQUS, *Eng. Fract. Mech.* 72 (2005) 2174–2185, doi:[10.1016/j.engfracmech.2005.02.003](https://doi.org/10.1016/j.engfracmech.2005.02.003).
- [104] S.A. Kim, W.L. Johnson, Elastic constants and internal friction of martensitic steel, ferritic-pearlitic steel, and  $\alpha$ -iron, *Mater. Sci. Eng. A* 452–453 (2007) 633–639, doi:[10.1016/j.msea.2006.11.147](https://doi.org/10.1016/j.msea.2006.11.147).
- [105] F.P.E. Dunne, D. Rugg, A. Walker, Lengthscale-dependent, elastically anisotropic, physically-based hcp crystal plasticity: application to cold-dwell fatigue in Ti alloys, *Int. J. Plast.* 23 (2007) 1061–1083, doi:[10.1016/j.jiplas.2006.10.013](https://doi.org/10.1016/j.jiplas.2006.10.013).
- [106] G.B. Arfken, H.J. Weber, F.E. Harris, in: *Rotation in R3. Mathematical Methods for Physicists: A Comprehensive Guide*, 7th ed., Academic Press, 2013, pp. 139–141.
- [107] A. Melcher, A. Unser, M. Reichhardt, B. Nestler, M. Pötschke, M. Selzer, Conversion of EBSD data by a quaternion based algorithm to be used for grain structure simulations, *Tech. Mech.* (2010) 30.
- [108] Ben-Ari M.A Tutorial on Euler angles and quaternions. 2014.
- [109] W.L. Bond, The mathematics of the physical properties of crystals, *Bell Syst. Tech. J.* 22 (1943) 1–72, doi:[10.1002/j.1538-7305.1943.tb01304.x](https://doi.org/10.1002/j.1538-7305.1943.tb01304.x).
- [110] T.B. Britton, J. Jiang, Y. Guo, A. Vilalta-Clemente, D. Wallis, L.N. Hansen, et al., Tutorial: crystal orientations and EBSD – or which way is up? *Mater. Charact.* 117 (2016) 113–126, doi:[10.1016/j.matchar.2016.04.008](https://doi.org/10.1016/j.matchar.2016.04.008).
- [111] S.G. Lekhnitskii, General equations of the theory of elasticity of an anisotropic body, in: *Theory of Elasticity of an Anisotropic Elastic Body*, 1st ed., MIR Publishers, Moscow, 1981, pp. 15–73.
- [112] E. Salvati, T. Sui, A.M. Korsunsky, Uncertainty quantification of residual stress evaluation by the FIB–DIC ring-core method due to elastic anisotropy effects, *Int. J. Solids Struct.* 87 (2016) 61–69, doi:[10.1016/j.ijsolstr.2016.02.031](https://doi.org/10.1016/j.ijsolstr.2016.02.031).
- [113] B. Cotterell, J.R. Rice, Slightly curved or kinked cracks, *Int. J. Fract.* 16 (1980) 155–169, doi:[10.1007/BF00012619](https://doi.org/10.1007/BF00012619).
- [114] R.A. Schwarzer, J. Hjelen, Backscattered electron imaging with an EBSD detector, *Microsc. Today* 23 (2015) 12–17, doi:[10.1017/S1551929514001333](https://doi.org/10.1017/S1551929514001333).
- [115] D.M. Saylor, B.S. El-Dasher, B.L. Adams, G.S. Rohrer, Measuring the five-parameter grain-boundary distribution from observations of planar sections, *Mettall. Mater. Trans. A* 35 (2004) 1981–1989, doi:[10.1007/s11661-004-0147-z](https://doi.org/10.1007/s11661-004-0147-z).
- [116] B.A. El, A. Véronique, S. Degallaix, Surface observation and measurement techniques to study the fatigue damage micromechanisms in a duplex stainless steel, *Int. J. Fatigue* 31 (2009) 2049–2055, doi:[10.1016/j.ijfatigue.2008.11.003](https://doi.org/10.1016/j.ijfatigue.2008.11.003).
- [117] R. Hielscher, H. Schaeben, A novel pole figure inversion method: specification of the MTEX algorithm, *J. Appl. Crystallogr.* 41 (2008) 1024–1037, doi:[10.1107/S0021889808030112](https://doi.org/10.1107/S0021889808030112).
- [118] R. Jiang, F. Pierron, S. Octaviani, P.A.S. Reed, Characterisation of strain localisation processes during fatigue crack initiation and early crack propagation by SEM–DIC in an advanced disc alloy, *Mater. Sci. Eng. A* 699 (2017) 128–144, doi:[10.1016/j.msea.2017.05.091](https://doi.org/10.1016/j.msea.2017.05.091).
- [119] J.H. Kuang, Y.C. Chen, The values of *J*-integral within the plastic zone, *Eng. Fract. Mech.* 55 (1996) 869–881, doi:[10.1016/S0013-7944\(96\)00077-X](https://doi.org/10.1016/S0013-7944(96)00077-X).
- [120] Systèmes® D. ABAQUS. ABAQUS v66 2009. <https://classes.engineering.wustl.edu/2009/spring/mase5513/abaqus/docs/v6.6/index.html>.
- [121] W. Niblack, *An Introduction to Digital Image Processing*, Strandberg Publishing Company, 1985 DNK.
- [122] J.C. Fisher, E.W. Hart, R.H. Pry, Theory of slip-band formation, *Phys. Rev.* 87 (1952) 958–961, doi:[10.1103/PhysRev.87.958](https://doi.org/10.1103/PhysRev.87.958).
- [123] J. Du, F. Mompioni, W.Z. Zhang, *In-situ* TEM study of dislocation emission associated with austenite growth, *Scr. Mater.* 145 (2018) 62–66, doi:[10.1016/j.scriptamat.2017.10.014](https://doi.org/10.1016/j.scriptamat.2017.10.014).



- [124] K.Y. Xie, Y. Wang, S. Ni, X. Liao, J.M. Cairney, S.P. Ringer, Insight into the deformation mechanisms of  $\alpha$ -Fe at the nanoscale, *Scr. Mater.* 65 (2011) 1037–1040, doi:[10.1016/j.scriptamat.2011.08.023](https://doi.org/10.1016/j.scriptamat.2011.08.023).
- [125] D. Kiener, A.M. Minor, Source-controlled yield and hardening of Cu(100) studied by *in situ* transmission electron microscopy, *Acta Mater.* 59 (2011) 1328–1337, doi:[10.1016/j.actamat.2010.10.065](https://doi.org/10.1016/j.actamat.2010.10.065).
- [126] F.C. Frank, W.T. Read, Multiplication processes for slow moving dislocations, *Phys. Rev.* 79 (1950) 722–723, doi:[10.1103/PhysRev.79.722](https://doi.org/10.1103/PhysRev.79.722).
- [127] D. Howell, I.G. Wood, D.P. Dobson, A.P. Jones, L. Nasdala, J.W. Harris, Quantifying strain birefringence halos around inclusions in diamond, *Contrib. Mineral. Petrol.* 160 (2010) 705–717, doi:[10.1007/s00410-010-0503-5](https://doi.org/10.1007/s00410-010-0503-5).
- [128] J.W. Hutchinson, Singular behaviour at the end of a tensile crack in a hardening material, *J. Mech. Phys. Solids* 16 (1968) 13–31, doi:[10.1016/0022-5096\(68\)90014-8](https://doi.org/10.1016/0022-5096(68)90014-8).
- [129] J.R. Rice, G.F. Rosengren, Plane strain deformation near a crack tip in a power-law hardening material, *J. Mech. Phys. Solids* 16 (1968) 1–12, doi:[10.1016/0022-5096\(68\)90013-6](https://doi.org/10.1016/0022-5096(68)90013-6).
- [130] B.L. Adams, S.I. Wright, K. Kunze, Orientation imaging: the emergence of a new microscopy, *Metall. Trans. A* 24 (1993) 819–831, doi:[10.1007/BF02656503](https://doi.org/10.1007/BF02656503).
- [131] F.J. Humphreys, Review grain and subgrain characterisation by electron backscatter diffraction, *J. Mater. Sci.* 36 (2001) 3833–3854, doi:[10.1023/A:1017973432592](https://doi.org/10.1023/A:1017973432592).
- [132] A.J. Wilkinson, P.B. Hirsch, Electron diffraction based techniques in scanning electron microscopy of bulk materials, *Micron* 28 (1997) 279–308, doi:[10.1016/S0968-4328\(97\)00032-2](https://doi.org/10.1016/S0968-4328(97)00032-2).
- [133] H. Bei, S. Shim, M.K. Miller, G.M. Pharr, E.P. George, Effects of focused ion beam milling on the nanomechanical behavior of a molybdenum-alloy single crystal, *Appl. Phys. Lett.* 91 (2007) 111915, doi:[10.1063/1.2784948](https://doi.org/10.1063/1.2784948).
- [134] H. Bei, S. Shim, G.M. Pharr, E.P. George, Effects of pre-strain on the compressive stress-strain response of Mo-alloy single-crystal micropillars, *Acta Mater.* 56 (2008) 4762–4770, doi:[10.1016/j.actamat.2008.05.030](https://doi.org/10.1016/j.actamat.2008.05.030).
- [135] M.D. Uchic, P.A. Shade, D.M. Dimiduk, Plasticity of micrometer-scale single crystals in compression, *Annu. Rev. Mater. Res.* 39 (2009) 361–386, doi:[10.1146/annurev-matsci-082908-145422](https://doi.org/10.1146/annurev-matsci-082908-145422).
- [136] F. di Gioacchino, T.E.J. Edwards, G.N. Wells, W.J. Clegg, A new mechanism of strain transfer in polycrystals, *Sci. Rep.* 10 (2020) 1–15 2020 10:1, doi:[10.1038/s41598-020-66569-7](https://doi.org/10.1038/s41598-020-66569-7).
- [137] A. Koko, E. Elmukashfi, K. Dragnevski, A.J. Wilkinson, T.J. Marrow, J-integral analysis of the elastic strain fields of ferrite deformation twins using electron backscatter diffraction, *Acta Mater.* 218 (2021) 117203, doi:[10.1016/j.actamat.2021.117203](https://doi.org/10.1016/j.actamat.2021.117203).
- [138] Y. Xu, W. Wan, F.P.E. Dunne, Microstructural fracture mechanics: Stored energy density at fatigue cracks, *J. Mech. Phys. Solids* 146 (2021) 104209, doi:[10.1016/j.jmps.2020.104209](https://doi.org/10.1016/j.jmps.2020.104209).
- [139] X. Zhang, J.C. Stinville, T.M. Pollock, F.P.E. Dunne, Crystallography and elastic anisotropy in fatigue crack nucleation at nickel alloy twin boundaries, *J. Mech. Phys. Solids* 155 (2021) 104538, doi:[10.1016/j.jmps.2021.104538](https://doi.org/10.1016/j.jmps.2021.104538).
- [140] X. Su, W. Wan, F.P.E. Dunne, T.J. Marrow, Crack field analysis by optical DIC of short cracks in Zircaloy-4, *Procedia Struct. Integr.* 39 (2022) 663–670, doi:[10.1016/j.PROSTR.2022.03.139](https://doi.org/10.1016/j.PROSTR.2022.03.139).
- [141] A. Koko, T.H. Becker, E. Elmukashfi, N.M. Pugno, A.J. Wilkinson, T.J. Marrow, HR-EBSD analysis of *in situ* stable crack growth at the micron scale, *J. Mech. Phys. Solids* (2022) (Under Review), doi:[10.48550/arXiv.2206.10243](https://doi.org/10.48550/arXiv.2206.10243).
- [142] Y. Mikami, K. Oda, M. Kamaya, M. Mochizuki, Effect of reference point selection on microscopic stress measurement using EBSD, *Mater. Sci. Eng. A* 647 (2015) 256–264, doi:[10.1016/j.msea.2015.09.004](https://doi.org/10.1016/j.msea.2015.09.004).
- [143] P. Jenčuš, J. Polák, P. Lukáš, O. Muránsky, *In situ* neutron diffraction study of the low cycle fatigue of the  $\alpha$ - $\gamma$  duplex stainless steel, *Physica B* 385–386 (2006) 597–599, doi:[10.1016/j.physb.2006.06.109](https://doi.org/10.1016/j.physb.2006.06.109).
- [144] A.A. MacDowell, R.S. Celestre, N. Tamura, R. Spolenak, B. Valek, W.L. Brown, et al., Submicron X-ray diffraction, *Nucl. Instrum. Methods Phys. Res. A* 467–468 (2001) 936–943, doi:[10.1016/S0168-9002\(01\)00530-7](https://doi.org/10.1016/S0168-9002(01)00530-7).
- [145] Y. Guo, D.M. Collins, E. Tarleton, F. Hofmann, J. Tischler, W. Liu, et al., Measurements of stress fields near a grain boundary: exploring blocked arrays of dislocations in 3D, *Acta Mater.* 96 (2015) 229–236, doi:[10.1016/j.actamat.2015.05.041](https://doi.org/10.1016/j.actamat.2015.05.041).
- [146] Y. Guo, D.M. Collins, E. Tarleton, F. Hofmann, A.J. Wilkinson, T. Britton, Dislocation density distribution at slip band-grain boundary intersections, *Acta Mater.* 182 (2020) 172–183, doi:[10.1016/j.actamat.2019.10.031](https://doi.org/10.1016/j.actamat.2019.10.031).
- [147] M. Kutsal, P. Bernard, G. Berruyer, P.K. Cook, R. Hino, A.C. Jakobsen, et al., The ESRF dark-field x-ray microscope at ID06, *IOP Conf. Ser. Mater. Sci. Eng.* 580 (2019) 12007, doi:[10.1088/1757-899x/580/1/012007](https://doi.org/10.1088/1757-899x/580/1/012007).
- [148] H. Yu, J. Liu, P. Karamched, A.J. Wilkinson, F. Hofmann, Mapping the full lattice strain tensor of a single dislocation by high angular resolution transmission Kikuchi diffraction (HR-TKD), *Scr. Mater.* 164 (2019) 36–41, doi:[10.1016/j.scriptamat.2018.12.039](https://doi.org/10.1016/j.scriptamat.2018.12.039).
- [149] M.J. McLean, W.A. Osborn, *In-situ* elastic strain mapping during micromechanical testing using EBSD, *Ultramicroscopy* 185 (2018) 21–26, doi:[10.1016/j.ultramic.2017.11.007](https://doi.org/10.1016/j.ultramic.2017.11.007).
- [150] W. Zielinski, M.J. Lii, W.W. Gerberich, Crack-tip dislocation emission arrangements for equilibrium – I. *In situ* TEM observations of Fe2wt%Si, *Acta Metall. Mater.* 40 (1992) 2861–2871, doi:[10.1016/0956-7151\(92\)90451-J](https://doi.org/10.1016/0956-7151(92)90451-J).
- [151] T.J. Hardin, T.J. Ruggles, D.P. Koch, S.R. Niezgoda, D.T. Fullwood, E.R. Homer, Analysis of traction-free assumption in high-resolution EBSD measurements, *J. Microsc.* 260 (2015) 73–85, doi:[10.1111/jmi.12268](https://doi.org/10.1111/jmi.12268).